KfK 2553
März 1978

Numerical investigation of the influence of secondary flows on characteristic turbulence data

G. Grötzbach
Institut für Reaktorentwicklung
Projekt Schneller Brüter

Kernforschungszentrum Karlsruhe

KERNFORSCHUNGSZENTRUM KARLSRUHE
Institut für Reaktorentwicklung
Projekt Schneller Brüter

KFK 2553

Numerical investigation of the influence of secondary flows on characteristic turbulence data

G. Grötzbach

Kernforschungszentrum Karlsruhe G.m.b.H., Karlsruhe

Abstract

A finite difference scheme is described for three-dimensional time dependent direct numerical simulation of turbulent velocity- and temperature fields in channel flows. The details of the subgrid scale models including wall roughness effects are discussed. The calculation of the turbulent flow through an infinite plane channel with one smooth and one rough wall is successfully used for the verification of the method. It is further successfully applied to a partly roughened channel to study the effect of secondary flows. The numerical results for the fluid air show, that the secondary flow is not only carrying momentum and heat, but also the velocity- and temperature fluctuations and the cross-correlation behaviour between velocity and temperature fluctuations. Thus a strong influence on the eddy diffusivities is detected. The turbulent Prandtl number seems to be unaffected.

Numerische Untersuchung des Einflusses von Sekundärströmungen auf charakteristische Daten der Turbulenz

Zusammenfassung

Es wird ein finites Differenzenverfahren zur 3-dimensionalen instationären direkten numerischen Simulation turbulenter Geschwindigkeits- und Temperaturfelder in Kanalströmungen beschrieben. Insbesondere diejenigen Teile der Feinstrukturmodelle werden diskutiert, die Wandrauhigkeitseffekte berücksichtigen. Zur Verifikation des Verfahrens wird die turbulente Strömung in einem unendlich ausgedehnten Plattenkanal mit einer glatten und einer rauhen Wand erfolgreich simuliert. Mit ähnlichem Erfolg wird das Verfahren auch auf einen Kanal mit teilweise rauhen Wänden zur Untersuchung der Auswirkung von Sekundärströmungen angewandt. Die Auswertung der numerischen Ergebnisse für das Fluid Luft zeigt, daß die Sekundärströmungen nicht nur Impuls und Wärme transportieren, sondern auch Geschwindigkeits- und Temperaturschwankungen. Überdies sind auch die Kreuzkorrelationseigenschaften zwischen Geschwindigkeits- und Temperaturschwankungen transportierbare Größen. Die turbulenten Austauschgrößen werden ebenfalls als transportierbar erkannt. Die turbulente Prandtl-Zahl scheint von den Sekundärströmungen nicht beeinflußt zu werden.

List of Contents

List of figures

List of tables

1. Introduction

The method of direct numerical simulation of turbulent flows is based on the entire time-dependent, three-dimensional equations for mass, momentum and heat. Using finite difference grids with finite spatial resolution, sub-grid scale models are required for the consideration of the momentum and heat transport within the grid cells. Turbulence-elements which are greater than a few grid cells are simulated directly. Therefore, all those turbulence quantities may be calculated from the numerical results, which are largely dominated by the gross-scale turbulence.

For turbulent channel flows this method was used for the first time by Deardorff [1]. The method was extended by Schumann [2] for application to non-equidistant meshes, to finite Reynolds-numbers and to a more realistic consideration of the sub-grid scale fluxes in the near wall region. Further extensions [3] relate to the applicability to low Reynolds-number flows, coarse grids, rough walls and additional simulation of the temperature field. Thus the accuracy of the numerical results becomes comparable to experimental data, even if rather coarse grids are used and short time intervalls are calculated [3, 4]. Studying the turbulent temperature fields of the flow of liquid metals with very small molecular Prandtl-numbers, the method has some advantages compared to experiments [3, 5] especially with regard to accuracy.

Because of these advantages, the method of direct numerical simulation provides a good possibility to study the effect of secondary currents, which occur in many technical flow problems like in rectangular or square ducts, eccentric annuli, or in fuel elements of nuclear reactors. Some of the models usually used to calculate the detailed flow in such geometries do not include secondary flows, but only non-isotropic eddy diffusivities [6, 7]. Some include secondary flows, but use eddy diffusivities which do not depend on the secondary flow [8, 9]. In some models additional approximative transport equations are used for all Reynolds stresses [10]. Nevertheless all models are of modeste accuracy. This is due to the large number of unknown 'constants' included in the models. By appropriate estimation of these 'constants' from proper experimental results [11 - 14] one can reproduce similar numerical results with very different models. But the same values of the 'constants' may not be used for other types of flows or geometries. The models are therefore not universal.

In this paper the method of direct numerical simulation using sub-grid scale models is shortly discussed, as realized in the computer code TURBIT-2 (Turbulenter Impuls Transport) /¯3_7. It will be shown which parts of the model account for wall roughness effects. The main purpose is to present some numerical results for turbulent flows through partly roughened plane channels with and without secondary flow. Thereby we find it as a further advantage of the method that the instantaneous velocities, pressure and temperature values are known in each grid cell at the same time.

2. Basic equations of the direct numerical simulation method

2.1 Averaged conservation equations

The method of direct numerical simulation presented in this paper is based on a finite difference scheme which solves the Navier-Stokes equation, the continuity and the thermal energy equations. For the deduction of this scheme the basic equations are averaged over finite grid volumes $V = \Delta x_1 \cdot \Delta x_2 \cdot \Delta x_3$:

$$ {}^{V}\overline{y} = \frac{1}{\Delta x_1 \Delta x_2 \Delta x_3} \int_{\Delta x_1} \int_{\Delta x_2} \int_{\Delta x_3} y(x_1', x_2', x_3')\, dx_3'\, dx_2'\, dx_1' \tag{1} $$

$$ {}^{V}\overline{\frac{\partial y}{\partial x_1}} = \frac{1}{\Delta x_1} \left[{}^{1}\overline{y}\left(x_1 + \frac{\Delta x_1}{2}\right) - {}^{1}\overline{y}\left(x_1 - \frac{\Delta x_1}{2}\right) \right] = \delta_1\, {}^{1}\overline{y} \tag{2} $$

Hereby, the triple integral defining the average ${}^{V}\overline{y}$ (1) is integrated by parts with respect to the divergence type terms (2) so that the average is expressed in terms of finite differences of surface mean values ${}^{i}\overline{y}$ [2]. This allows using grid cells with different spacings Δx_i. The resultant equations are the averaged mass, or continuity equation (3), the averaged momentum, or Navier-Stokes equation (4) and the averaged thermal energy equation (5), where $\dot{Q}$ is the volumetrical heat source within the fluid:

$$ \delta_i\, {}^{i}\overline{u_i} = 0 \tag{3} $$

$$ \frac{\partial}{\partial t}\, {}^{V}\overline{u_i} = -\delta_j\, {}^{j}\overline{u_i}\, {}^{j}\overline{u_j} - \delta_j\, {}^{j}\overline{u_i' u_j'} - \delta_i\, {}^{i}\overline{p} + \delta_j \left(\nu\, {}^{j}\overline{\frac{\partial u_i}{\partial x_j}} \right) + \delta_{1i} P_x \tag{4} $$

$$ \frac{\partial}{\partial t}\, {}^{V}\overline{T} = -\delta_j\, {}^{j}\overline{u_j}\, {}^{j}\overline{T} - \delta_j\, {}^{j}\overline{u_j' T'} + \delta_j \left(a\, {}^{j}\overline{\frac{\partial T}{\partial x_j}} \right) + \dot{Q} \tag{5} $$

Regarding to repeated lower indices the summation convention is assumed. The geometry and the coordinate system are shown in Fig. 1. The x_1-direction corresponds to the direction of the time mean velocity and pressure

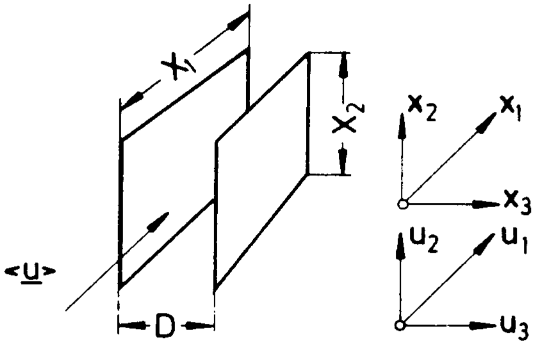

Fig. 1:
Channel geometry

gradient $P_x = 2$ of the infinite plane channel. The x_3-direction is perpendicular to the walls. All quantities of equations (3) to (5) are made dimensionless by means of the channel width $\hat{D}$, the friction velocity $\overline{\hat{u}_\tau} = (\overline{\hat{\tau}_w}/\hat{\rho})^{1/2}$ ($\overline{\hat{\tau}_w}$ = time mean wall shear stress, averaged over both walls, $\hat{\rho}$ = constant density), and the heat flux temperature $\overline{\hat{T}^x} = \overline{\hat{q}_w}/(\hat{\rho}\ \hat{c}_p\ \overline{\hat{u}_\tau})$ ($\overline{\hat{q}_w}$ = time mean wall heat flux, averaged over both walls, $\hat{c}_p$ = constant specific heat capacity). The dimensionless diffusivities are $\nu = \hat{\nu}/(\overline{\hat{u}_\tau}\cdot\hat{D}) = 1/Re_\tau$ and $a = 1/(Re_\tau Pr)$. By using the friction coefficient c_f we get the common Reynolds-number:

$$Re = Re_\tau\ (\hat{u}_b/\overline{\hat{u}_\tau}) = Re_\tau\sqrt{8/c_f} \qquad (6)$$

2.2 Subgrid scale flux approximations

No approximations have been so far involved. However equations (3-5) are yet unclosed. For the unknown subgrid scale (SGS) fluxes of momentum ${}^j\overline{u'_i u'_j}$ and heat ${}^j\overline{u'_j T'}$ special subgrid scale models are introduced which are appropriate for channel flows with smooth and rough walls and for channels with and without secondary flows [3].

First, according to [2], the SGS-fluxes are split formally into a fluctuating locally isotropic part and a time mean inhomogeneous part.

Secondly, for both parts gradient diffusion is assumed, analogues to the molecular diffusion:

$$ {}^{j}\overline{u'_i u'_j} = - {}^{ij}\mu \, (D_{ij} - \langle D_{ij} \rangle) - {}^{ij}\mu^{*} \langle D_{ij} \rangle \tag{7} $$

$$ {}^{j}\overline{u'_j T'} = - {}^{j}a_t \, \delta_j \, ({}^{j}\overline{T} - \langle {}^{j}\overline{T} \rangle) - {}^{j}a_t^{*} \, \delta_j \langle {}^{j}\overline{T} \rangle \tag{8} $$

where

$$ D_{ij} = \partial u_i / \partial x_j + \partial u_j / \partial x_i \tag{9} $$

and $\langle D_{ij} \rangle$ is the time mean value of (9). The unknown eddy diffusivities ${}^{ij}\mu$ and ${}^{ij}\mu^{*}$, and eddy conductivities ${}^{j}a_t$ and ${}^{j}a_t^{*}$ are calculated from modified common turbulence models:

The isotropic eddy diffusivities ${}^{ij}\mu$ are determined by a Prandtl-energy-length-scale-type model [2]. The isotropic eddy conductivities ${}^{j}a_t$ are modeled in an analogues manner, assuming that the subgrid scale heat flux depends on the velocity fluctuations within the grid cells [3]:

$$ {}^{ij}\mu = C_2 \; {}^{ij}C \; ({}^{j}F \; {}^{j}C_5 \; {}^{v}\overline{E'})^{1/2} \tag{10} $$

$$ {}^{j}a_t = C_{T2} \; {}^{j}C_T \; ({}^{j}F \; {}^{j}C_5 \; {}^{v}\overline{E'})^{1/2} \tag{11} $$

Here the characteristic length scale is the surface area ${}^{j}F$ of the grid cell over which the averages (7 and 8) are defined, and the characteristic energy is the SGS-kinetic energy ${}^{v}\overline{E'}$ of the not resolved velocity fluctuations (see chapter 2.3).

The coefficients ${}^{j}C_5$, ${}^{ij}C$ and ${}^{j}C_T$ account for geometrical details of the mesh and the finite difference scheme and are of order one. Because of the formal splitting (7, 8) of the SGS-fluxes, these coefficients, and the dominating coefficients C_2 and C_{T2}, may be determined theoretically under the assumption of locally isotropic subgrid scale turbulence [3]. To this purpose we assume the validity of the well-known Kolmogorov spectra for the kinetic energy and temperature variances.

The inhomogeneous eddy diffusivities ${}^{ij}\mu^{*}$ and eddy conductivities ${}^{j}a_t^{*}$ are derived from modified common mixing length models [3]:

$$ {}^{ij}\mu^{*} = \delta_{1i}\;\delta_{3j}\;l^{2}\left|\left\langle {}^{V}\overline{\frac{\partial u_i}{\partial x_3}} \right\rangle\right|\; f\,(C_{1o},\,\Delta x_i) \tag{12} $$

$$ {}^{j}a_t^{*} = \delta_{3j}\;\;l\;\;l_H\left|\left\langle {}^{V}\overline{\frac{\partial T}{\partial x_3}} \right\rangle\right|\; f_H\,(C_{T1o},\,\Delta x_i) \tag{13} $$

The mixing lengths l and l_H are well-known functions of the distance y from the wall and the dimensional wall roughness $h^{+} = h \cdot Re_{\tau}$ (h = height of sand grain roughness). In addition l_H depends on the molecular Prandtl number of the fluid. We use a Nikuradse-Van Driest, and Cebeci formulation respectively [3, 15]:

$$ l = f_l\,(y,\,h^{+}) \tag{14} $$

$$ l_H = f_{lH}(y,\,Pr) \tag{15} $$

The crucial factors in (12, 13) are the damping functions f and f_H. They are designed so that for very coarse meshes the SGS-models become equal to the common models for time averaged turbulence (f, $f_H \equiv 1$). For very fine resolution the functions vanish (f, $f_H \rightarrow 0$) since in this case all SGS-fluxes are described by the isotropic parts. These functions have been adjusted numero-empirically once for all cases [3].

2.3 Additional SGS-energy equation

The characteristic energy used in the isotropic parts (10, 11) of the SGS-flux models is the subgrid scale kinetic energy ${}^{V}\overline{E'} = \frac{1}{2}\;{}^{V}\overline{(u_i - {}^{V}\overline{u_i})^{2}}$. It is calculated using an additional time dependent three-dimensional transport equation as deduced in [2]:

$$ \frac{\partial\,{}^{V}\overline{E'}}{\partial t} = \text{Production} + \text{Diffusion} - \text{Convection} - \text{Dissipation} \tag{16} $$

To get a consistent formulation and a better physical behaviour of the isotropic equation used in [2] it is necessary [3] to include inhomogenuity effects in the production and dissipation terms. For the SGS-flux in the production term

$$ \text{Production} = -\,{}^{j}\overline{u_i'\,u_j'}\;\;\delta_j\;{}^{j}\overline{u_i} \tag{17} $$

now not only the isotropic part is used, but also the inhomogeneous part of equation (7). This means that all energy dissipated in the SGS-flux model from the large scale structure appears in the subgrid scale structure. According to equations (12, 14) the production is now influenced directly by the wall roughness h^+. (In the final finite difference form of the production term the additional theoretically determined coefficient $C_{2o} = C_4/C_2$ /¯2, 3_7 corrects some further required finite difference approximations.)

The extended model for the SGS-dissipation ${}^{V}\overline{\varepsilon^{T}}$ accounts also for inhomogenuity and roughness effects. In addition it allows the application of the method to smaller Reynolds numbers ($Re > 10^4$) and coarser grids. We use the following Rotta-type formulation /¯3, 4_7:

$$ {}^{V}\overline{\varepsilon^{T}} = C_3 \, {}^{V}\overline{E^{T}}^{3/2}/\mathrm{Min}(h, C_{31} l) + C_{32} \, \nu \, {}^{V}\overline{E^{T}} / \mathrm{Min}(h, C_{31} l)^2 \qquad (18) $$

$$ h = (\Delta x_1 \, \Delta x_2 \, \Delta x_3)^{1/3} \qquad (19) $$

The first term is dominant at large Reynolds numbers, while the second term at small Reynolds numbers. The minimum function gives the grid size h as a characteristic length scale in the core of the flow, and the mixing length l (14) in the near wall region. For the determination of the coefficient C_3 and of the constants $C_{31} = 0.74$ and $C_{32} = 20.0$ see /¯3_7.

2.4 Boundary conditions

In the x_1- and the x_2-direction it has been assumed periodicity with periodic lengths X_1 and X_2 (Fig. 1). In the x_3-direction, the normal velocity has been set to zero at the walls. Regarding to the x_1-direction the time dependent wall shear stresses $\tau_{wi} = -\nu \, {}^{3}\overline{\partial u_1/\partial x_3}$ are computed from the proportion /¯2_7:

$$ \frac{\tau_{wi}}{\langle \tau_{wi} \rangle} \simeq \left. \frac{{}^{1}\overline{u}_1}{\langle {}^{1}\overline{u}_1 \rangle} \right| \text{wall adjacent grid cell.} \qquad (20) $$

From experiments [16] it is known that there is a phase lag between u_1 and τ_{wi}. The phase lag is not explicitely included in equation (20), but the present model accounts for the time dependence of τ_{wi} which leads anyway to a better approximation than assuming $\tau_{wi} \approx \langle\tau_{wi}\rangle$. The time mean values $\langle\tau_{wi}\rangle$ are calculated from the actual and recent velocity fields by proper averaging of the universal logarithmic velocity profile [3]

$$u^+ = \frac{\langle u_1\rangle}{\langle\tau_{wi}\rangle^{1/2}} = \frac{1}{\kappa} \ln\,(y^+ E(h^+)) \tag{21}$$

over a grid cell in which the law of the wall is valid. For the Karman constant we use $\kappa = 0.4$. The wall roughness coefficient $E(h^+)$ in the logarithmic profile can be a function of the equivalent sand grain roughness height h^+ [15] and of the x_2-coordinate. This allows studying secondary flows caused by non-constant roughness.

The normal wall heat flux $\dot{q}_{wi} = -a\,\overline{{}^3\partial T/\partial x_3}$ is formulated in two different ways depending on the molecular Prandtl number Pr of the fluid. For very small Pr of liquid metals (Hg:Pr ≈ 0.02, Na:Pr ≈ 0.007) a linear approximation for the gradient in the wall heat flux has been used [3, 4]. For large Prandtl numbers a formulation has been used similar to (20):

$$\frac{\dot{q}_{wi}}{\langle\dot{q}_{wi}\rangle} = \left.\frac{{}^V\overline{T}-T_{wi}}{\langle{}^V\overline{T}-T_{wi}\rangle}\right|_{\text{wall adjacent grid cell}} \tag{22}$$

The time mean values $\langle\dot{q}_{wi}\rangle$ are calculated from the actual temperature field by proper averaging of the universal logarithmic temperature profile [3]:

$$T^+ = \frac{\langle T-T_{wi}\rangle}{\langle\dot{q}_{wi}\rangle}\,\langle\tau_{wi}\rangle^{1/2} = \frac{1}{\kappa_H}\,\ln y^+ + B_T(h^+, \mathrm{Pr}) \tag{23}$$

After extensive comparisons of experimental data the Karman constant for heat has been set to $\kappa_H = 0.465$ [3], and for the function $B_T(h^+, \mathrm{Pr})$ the theoretical approach of Dipprey and Sabersky [3, 15] has been followed.

Details of the finite difference scheme adapted to integrate the basic equations (3-5) in space and time are given in [3, 4]. Here the main features of the method of subgrid-scale modeling are discussed only with particular reference to the aspects including wall roughness effects. The inhomogeneous parts (12, 13) of the SGS-models, the production (17) and the dissipation terms (18) of the SGS-energy equation account for roughness effects by means of the mixing length (14). The formulation of the boundary conditions (20, 22) accounts for the wall roughness by using the universal logarithmic laws of the wall (21, 23). No special assumptions are added which refer to secondary flows. Therefore the results derived for the secondary currents do not reflect a peculiarity of the model or of the numerical method of solution but reflect a physical situation which is implicitely described by the full set of equations (3-5).

3. Numerical Results

Purpose of this section is first to demonstrate the general agreement between experiments and TURBIT-2 results for rough-walled channels. For smooth channels the agreement has been proven in [3, 4, 5] for plane channel and annular flows in a wide range of Reynolds and Prandtl numbers. Secondly we aim at showing the capability of this method to study the effect of secondary flows on typical turbulence data.

3.1 Plane channel flow with one constant roughened wall

For the verification of the code in the case of rough walled channels an experiment of Baumann [17] has been recalculated. The experiment was performed in a plane channel [18] with one rib-roughened wall. The measured velocity profiles were used to determine the equivalent sand-grain roughness height $h_1^+ = 465$. All input data used for the calculation of this test case, called K7, are listed in Tab. 1. The mesh contains

Tab. 1: Case specifications

	X_1	X_2	IM	JM	KM	Re	Pr	h_1^+	Problem time	no.of time steps	CPU-time IBM 370/168
K7 Baumann	2	1	16	8	16	194900	7	465	6.09 ÷ 9.54	1500	30 min
K8 Hinze	2	3	16	16	16	80000	0.7	180 0 180	6.57	2730	105 min

only 16·8·16 grid cells. The widths of the meshes are $\Delta x_1 = X_1/IM = 2/16$, $\Delta x_2 = X_2/JM = 1/8$, and $\Delta x_3 = 1/KM = 1/16$. In addition to this input data in both cases the wall roughness height at the second wall was set to $h_2^+ = 0$; the wall temperatures were $T_{wi} = 0$; the volumetrical heat source was set to $\dot{Q} = 2$ to obtain a stationary time mean temperature field. The subgrid scale coefficients calculated for the grid K7 and the corresponding Reynolds and Prandtl number with the method given in [3] are listed in Tab. 2. A sensitivity study has shown [3], that the theoretical values

Tab. 2: Theoretical values of the subgrid scale coefficients

SGS-coefficients	K7 - Baumann j = 1	2	3	K8 - Hinze j = 1	2	3
C_2	0.0755	-	-	0.0691	-	-
^{jj}C	1.5842	1.5842	1.4305	1.5621	1.7659	1.4570
^{1j}C	-	0.9813	0.7481	-	1.0245	0.6907
^{2j}C	-	-	0.7481	-	-	0.7608
$^{j}C_5$	0.7752	0.7752	0.9242	0.8379	0.6783	0.9438
C_{T2}	0.1753	-	-	0.1699	-	-
$^{j}C_T$	1.1317	1.1317	0.8112	1.0462	1.3295	0.7740
C_{2o}	0.8247	-	-	0.8395	-	-
C_3	0.5926	-	-	0.5553	-	-

of C_2 and C_{T2} are somewhat too large. Therefore in all cases C_2 and C_{T2} were divided by a factor $\gamma = 1.4$ instead of the previously used factor $\gamma = 3$ [2].

3.1.1 Time mean flow field

The time mean value of the velocity profile, calculated from the simulated time dependent velocity fields, is shown in Fig. 2. The computed profile is in very good agreement with the experimental data of Baumann [17], except in the near roughness region. This deviation may be due to the different types of roughnesses (rib roughness with recirculation zones behind the roughness elements in the experiment and sand grain roughness without resolved recirculation zones in the calculation) and due to the different types of variables compared: The experimental data are given as local mean values, while according to (1, 2), the numerical data are given as linear averaged surface mean values.

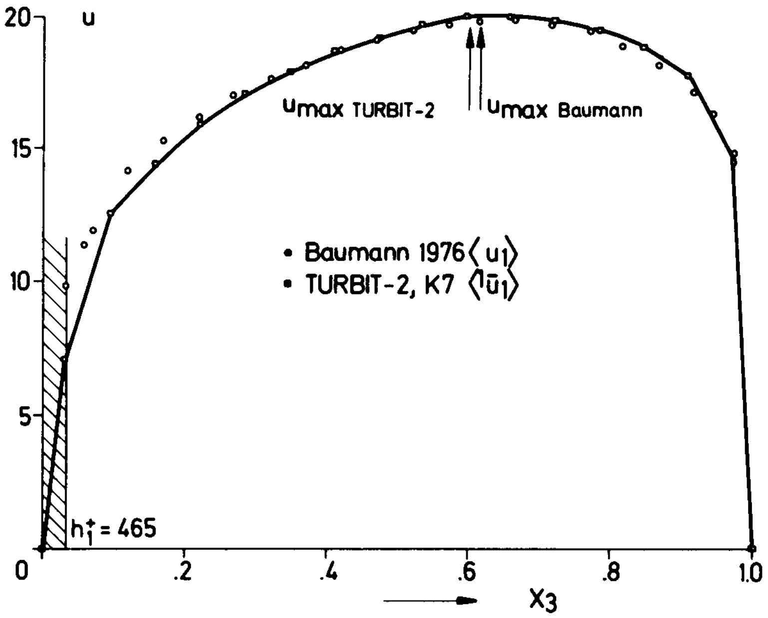

Fig. 2: Time mean velocity profile between the rough ($h_1^+ = 465$) and smooth ($h_2^+ = 0$) wall in the constant roughened channel

The logarithmic presentation of the time mean velocity profile near the rough wall shows a steeper increase than the averaged law of the wall (1,21). The resulting Karman constant is $\kappa_{rough} = 0.333$. This is in rather good qualitative and quantitative agreement with several experimental results of Baumann /¯17, 19_7.

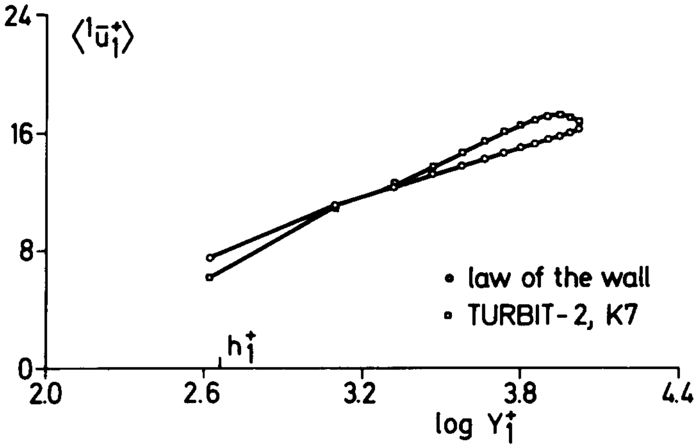

Fig. 3: Logarithmic presentation of the velocity profile near the rough wall

Tab. 3: Comparison of some characteristic numerical data with experimental data of Baumann [17]

	Baumann [17]	TURBIT-2, K7	Deviation
$\hat{u}_{1max}/\hat{u}_{\tau 1}$	16.53	17.25	+4 %
$\hat{u}_{1max}/\hat{u}_{\tau 2}$	24.72	25.7	+4 %
$\hat{u}_{1max}/\overline{\hat{u}_{\tau}}$	19.82	20.3	+2.5 %
c_f	0.0254	0.0267	+5,1 %
$y_{\tau=o}$	0.722	0.7	-3 %
y_{umax}	o.614	0.6	-2.3 %

The quantitative comparison of some characteristic data of the velocity profiles in Tab. 3 shows that the deviation of the maximum values of the velocities is only 2.5 %, and of the friction factor 5.1 %. The small positiv deviations of the numerical results from the experimental results are due to the simulation of the experimental finite plane channel with side walls with a in the x_2-direction infinite plane channel in the calculation [20]. The position of the maximum velocity is reproduced with comparable accuracy.

3.1.2 Statistics of the fluctuating flow field

Some typical vector- and contour-line plots are given in Fig. 4, which shows the instantaneous fields of the resolved fluctuating velocities, the total turbulence energy, the turbulent pressure, and the resolved fluctuating temperature. The main flow direction is from left to right. The lower boundary represents the roughened wall, the upper boundary the smooth wall. All the contour lines and velocity vectors show the known quasi-random behaviour. The velocity-, energy-, and temperature contour lines show some inclination against the flow direction towards the middle of the channel; this can be observed in all plots of this type [3, 4, 21]. As expected from experimental results [22] the

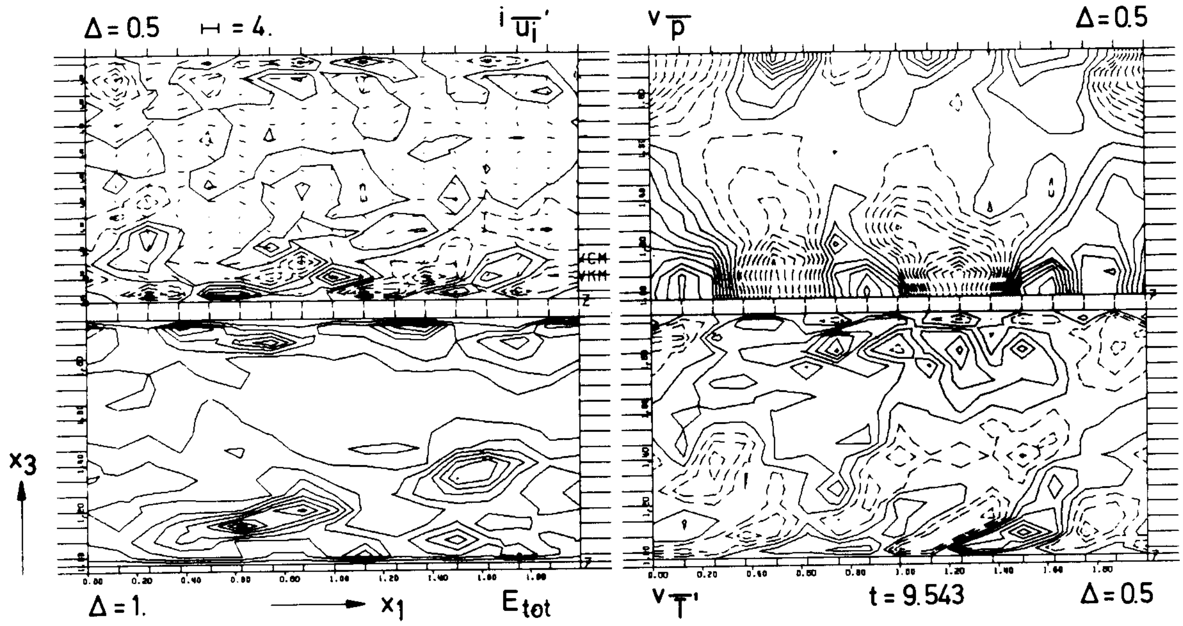

Fig. 4: Instantaneous resolved fluctuating velocities ${}^{i}\overline{u}_i' = {}^{i}\overline{u}_i - \langle {}^{i}\overline{u}_i \rangle$, total energy $E_{tot} = {}^{i}\overline{u}_i'^2/2 + {}^{v}\overline{E}'$, fluctuating pressure ${}^{v}\overline{p}$ and temperature ${}^{v}\overline{T}'$ in the K7-Baumann channel. Δ = contour line increment; dashed curves correspond to negative values.

fluctuations are larger near the roughened wall than near the smooth wall. A correlation between the pressure field and the other fields is not obvious. Indeed, the quantitative results for this cross-correlations are almost close to zero (see Fig. 16, 18 in the Appendix and [3]).

The root mean square values (rms) of the velocity fluctuations calculated from the simulated time-dependent velocity fiels are shown in Fig. 5. As remarked above the fluctuations are larger near the rough wall (x_3 = 0) than near the smooth wall (x_3 = 1) as concluded from Fig. 4. The minima are found between the locations of maximum velocity and of zero shear stress. No experimental data from Baumann are available for comparison. Some measurements of Hanjalič and Launder [22] have therefore been included to show the general agreement. The experimental data are transformed in such a way, that the minima appear at the same cross-stream position as the minima of the numerical results. This position has been

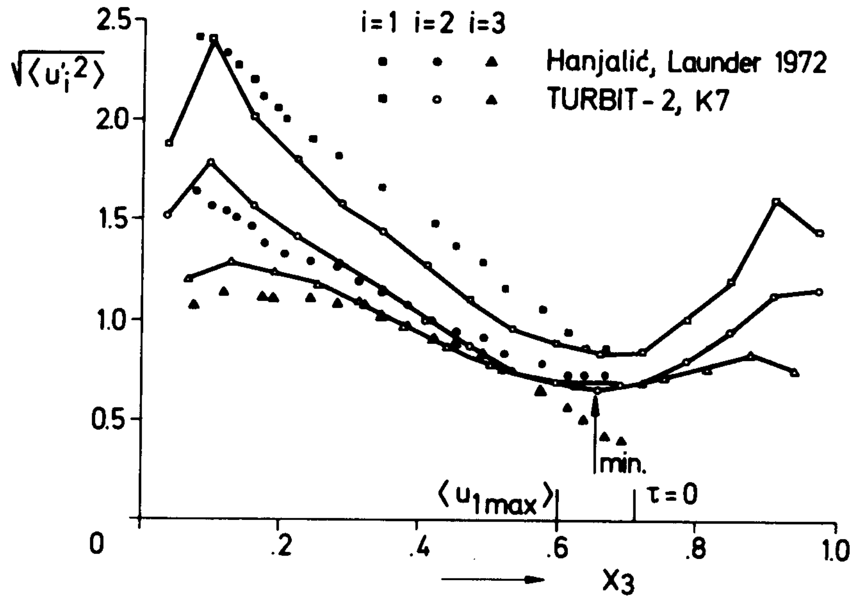

Fig. 5: Root-mean-square values of the velocity fluctuations $\sqrt{\langle u_i'^2 \rangle} = \sqrt{\langle {}^{i}\overline{u}_i'^2 \rangle + \frac{2}{3} \langle {}^{v}\overline{E}^{T} \rangle}$ in the K7-Baumann channel

found numerically to lay between the positions of maximum velocity and zero shear stress, perhaps nearer to the last one. This is in qualitative agreement with the experimental results of Rehme /¯23_7 for the non-symmetric flow through annuli with very small ratios of radii, or with the experimental results of Lawn /¯24_7 for smooth/rough annuli, but this is discordant to the experimental results of Hanjalić et al. /¯22_7. These experimental results are anyway not yet fully understood regarding to the behaviour of the rms-values of the x_3-component beyond the position of the minima.

The total turbulent shear stress is shown in Fig. 6 as sum of the directly resolved part and of the inhomogeneous part of the SGS-model (7, 12). The smaller computed values correspond to that part of the shear stress resolved directly by the large scale flow. With that, the major part of the momentum transport is accomplished by the resolved flow part. The shear stress distribution is not linear because of insufficient time averaging caused by the small computing time invested in this problem

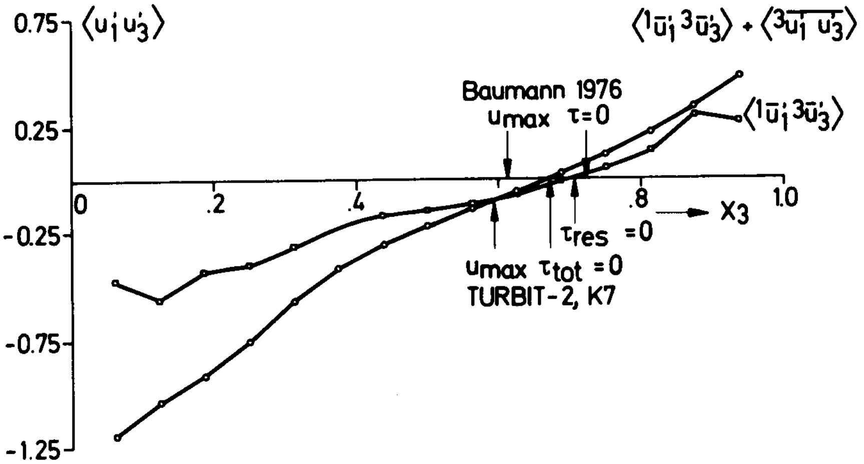

Fig. 6: The turbulent shear stress as sum of the directly resolved part $\tau_{res} = \langle {}^1\overline{u_1}' \, {}^3\overline{u_3}' \rangle$ and the inhomogeneous SGS-model $\langle {}^3\overline{u_1' u_3'} \rangle$

(Tab. 1). The position of the zero-crossing of the turbulent shear stress is calculated with an accuracy of 3 % (Fig. 6, Tab. 3). The small displacements are caused by the gradient-type SGS-model for the inhomogeneous part (12) of the SGS-shear stress. This part, and therefore the deviation as well, becomes smaller if grids with finer spatial resolution are used.

The analysis of the simulation of the turbulent flow through a plane channel with one roughened and one smooth wall has shown good agreement with the experimental results of Baumann. Not a single adjustment of additional correction factors has been required to tune the numerical results. Even using a rather coarse grid the accuracy of the numerical results is better than 5 % nevertheless. The accuracy of the numerical simulation of turbulent channel flows is therefore comparable to that of experiments.

3.2 Plane channel flow with one partly roughened wall

To study the consequences of secondary currents on characteristic turbulence data the turbulent flow through a channel with one smooth wall and one wall divided into rough and smooth stripes was calculated. The channel looks like that of Hinze [14], except for the infinity in the x_2-direction of the channel in the numerical simulation. As a consequence, the pattern of the secondary flow is not directly comparable. With this in mind, to save computing time the lateral periodicity length of the walls X_2 (Fig. 1) was reduced to $X_2 = 3$ (Tab. 1).

For the same reason the mesh width Δx_2 of the grid K8 was chosen to be $\Delta x_2 = X_2/JM = 3/16$ only. The data given by Hinze are not sufficient to estimate an equivalent sand-grain roughness height h^+ for the rough stripes. The numerical results will therefore be comparable only in a qualitative manner with the channel data of Hinze [14]. Further input data for the simulation are summarized in Tab. 1. The theoretical values of the subgrid scale coefficients are given in Tab. 2. (Some of the following numerical results have also been published in [25].)

3.2.1 Discussion of the flow field

In Fig. 7 vector- and contour-line plots are given for the time averaged fields of the velocities, the temperature, the resolved parts of the turbulent shear stresses and heat fluxes. The main stream direction is perpendicular to the plots. The roughness discontinuities at the lower wall cause secondary currents in the plane perpendicular to the mean velocity, which are represented by the vectors. For instance in the plane of symmetry in the smooth region the secondary flow carries fluid of low momentum and temperature from the cooled walls in the cross-stream direction to the middle of the channel. By that means the maxima of mean velocity and temperature do not appear in this region. These maxima are rather found near the boundaries between the smooth and rough stripes in regions, in which the secondary flow is almost zero. In the rough region the secondary flow carries fluid of high momentum from the near smooth wall region to the near rough wall region.

The velocity field calculated by time averaging the simulated turbulence fields is in good qualitative agreement with the experiments of Hinze /¯14_7. For the temperature field no comparable experimental data are available. But the experimental results from Kirsch /¯26, 27_7 for the temperature field behind blockages in fuel elements of nuclear reactors indicate that the position of maximum temperature should be in a region of very small secondary flow, which agrees with the numerical result.

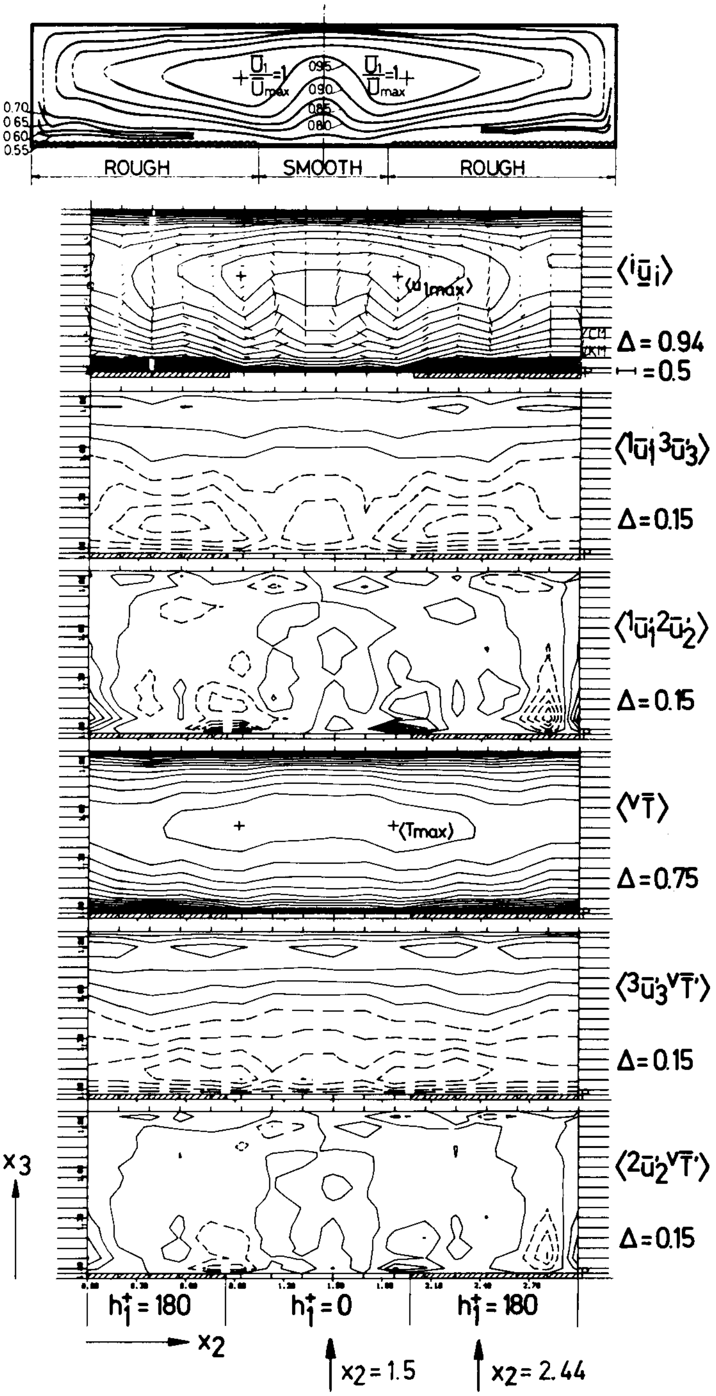

Reprinted from Hinze /¯14_7

Fig. 7: Vector- and contour-line plots of the resolved time mean velocities $<{}^{i}\overline{u_i}>$, shear stresses $<{}^{1}\overline{u_1}', {}^{j}\overline{u_j}'>$, temperature $<{}^{V}\overline{T}>$ and heat fluxes $<{}^{j}\overline{u_j}', {}^{V}\overline{T}'>$. The lower wall is divided into rough (h_1^+ = 180) and smooth (h_1^+ = 0) stripes. Δ = contour-line increment; dashed courves correspond to negative values.

The isolines of the resolved part of the radial turbulent shear stress $<^3\overline{u_3'\ ^1u_1'}>$ and heat flux $<^3\overline{u_3'\ ^vT'}>$ show regions of nearly constant values especially near the lower wall. Some of the isolines are even parallel to the secondary flow vectors. This behaviour is not so obvious at the lateral turbulent shear stress $<^2\overline{u_2'\ ^1u_1'}>$ and heat flux $<^2\overline{u_2'\ ^vT'}>$, which is mainly dominated by extrema at positions at which the mean flow or temperature field shows larger lateral gradients. Except for these two plots most of the isolines are distorted in the direction of the secondary flow. It is therefore supposed that the secondary flow is not only carrying momentum and heat, but also other turbulence data like the turbulent shear stress and heat flux.

3.2.2 Velocity statistics

Several cross stream profiles are given below for the lateral positions x_2 = 1.5 (smooth) and x_2 = 2.44 (rough). The mean velocity profile (Fig. 8) in the rough region is somewhat more symmetrical than in the smooth region.

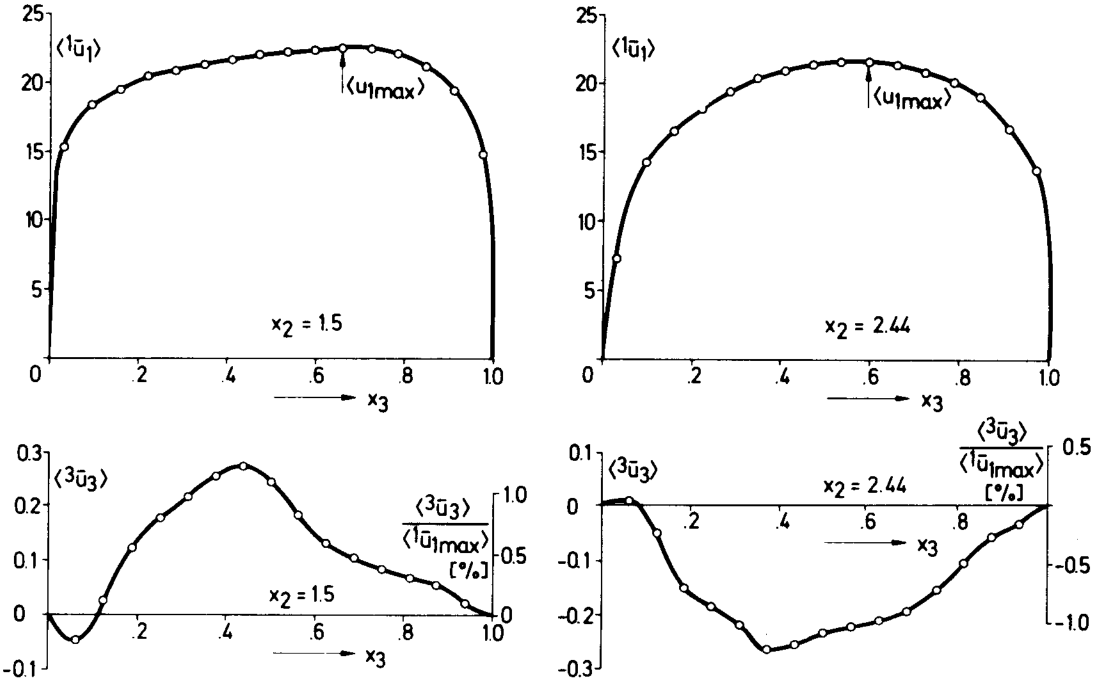

Fig. 8: Main and cross-stream velocities in the smooth (x_2 = 1.5) and rough regions (x_2 = 2.44)

This behaviour is contradictory to that obtained without secondary flow at an even larger wall roughness height (see Fig. 2). The reason is that the cross stream velocity $\langle u_3 \rangle$ carries fluid of low momentum from the rough region to the smooth region and vice versa. The prediction of a partly linear and not symmetrical profile in the plane of symmetry is consistent with the results of Hinze [14]. The calculated secondary flow is smaller by a factor of 3. This is mainly a consequence of the infinite plane channel and a too small equivalent sand-grain roughness. (The roughness height which has been chosen here results in an over all friction coefficient $c_f = 0.0214$ and a Nusselt number $Nu_D = 150.4$.) Nevertheless all results of Hinze can be verified sufficiently.

The above conclusion applies also to the rms-values of the velocity fluctuations (Fig. 9), which show the same symmetrical behaviour as the

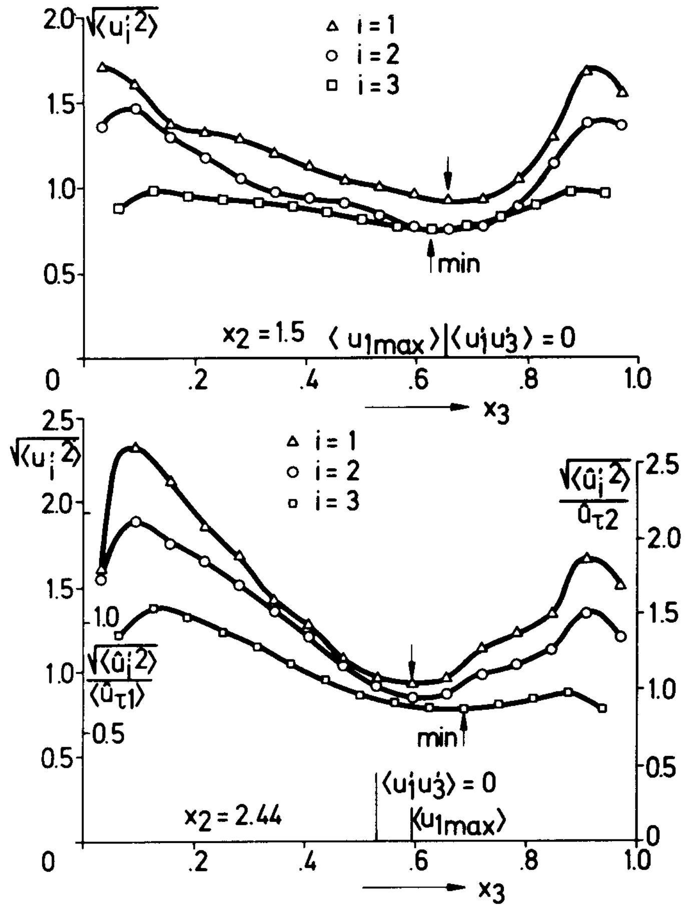

Fig. 9:

Root-mean-square velocity fluctuations $\sqrt{\langle u_i'^2 \rangle} = \sqrt{\langle \overline{u_i'^2} \rangle + 2/3 \langle {}^V E' \rangle}$ in the smooth ($x_2 = 1.5$) and rough ($x_2 = 2.44$) regions of the K8-Hinze channel.

mean velocity. The fluctuations are larger near the rough wall, than near the smooth wall, which is consistent with Fig. 5, but they are of comparable magnitude if normalized with the local wall shear stress. The minima are mainly located between the points of maximum velocity and zero shear stress.

The radial turbulent shear stress shows a similar behaviour (Fig. 10). The shear stress profile is strongly non linear, so that for example the point of zero shear stress in the smooth part of the channel (near the plane of symmetry) is not to be found in the middle of the channel, also the wall shear stresses $|\tau_{wi}|$ at both walls are nearly equal. The curvature of the shear stress profiles is directly connected with the direction of the cross stream velocity u_3 (Fig. 8).

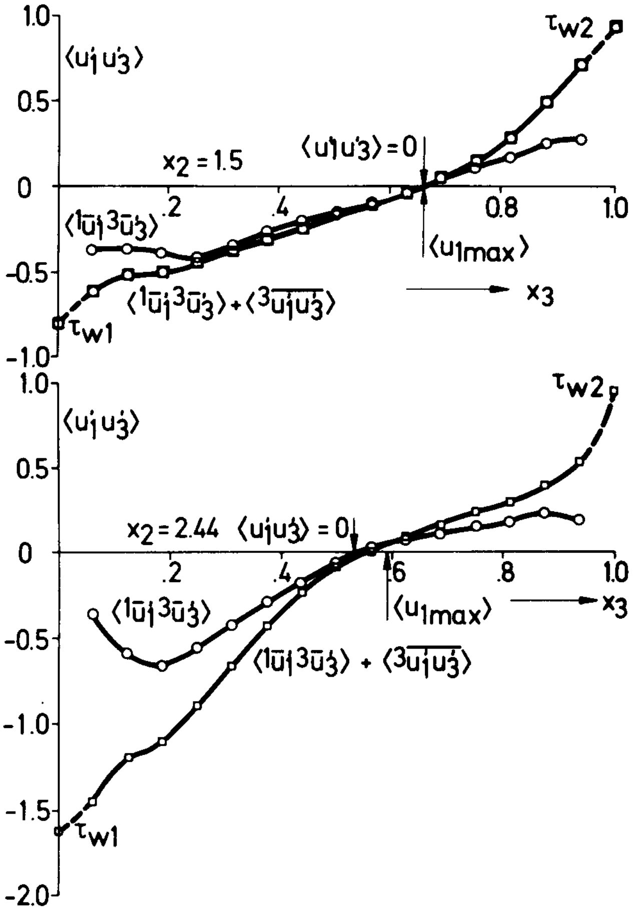

Fig. 10:
Radial turbulent shear stress $<u_1' \; u_3'>$ as sum of the directly resolved part $< {}^1\overline{u_1}', \; {}^3\overline{u_3}'>$ and the time mean part of the SGS model.

Thus one can verify that the secondary flow is not only carrying momentum, but also the kinetic energy of the velocity fluctuations, here represented by the rms-values, and the cross-correlation behaviour between several velocity fluctuations, here represented by the turbulent shear stress. The existence of distortions in these fields is therefore an additional indication for the existence of secondary flows, as assumed by the interpretation of experimental results in [28, 29]. The reason for this pronounced transport behaviour seems to lay in the slow build up (over large distances) [3, 30] and just so slow reduction [30] of these physical quantities.

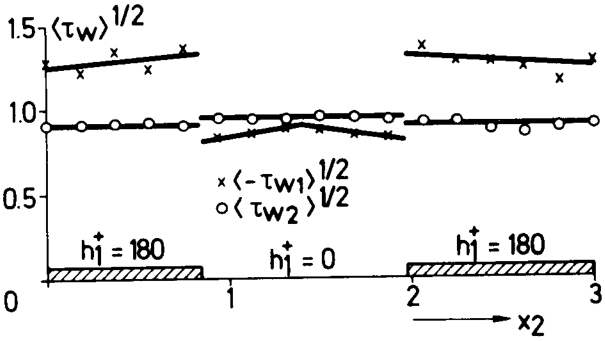

Fig. 11:
Wall shear stress profile at the partly roughened wall W1 and smooth wall W2.

Because of the coarse grid no data are available for the nearest region to the wall. From the lateral wall shear stress profile (Fig. 11), calculated from the numerical results by using grid cell averaged logarithmic velocity profiles (1,21), one can see that there is no strong influence of the secondary flow. As found experimentally by Wang and Nickerson [13] the wall shear stress shows sharp jumps at the positions of the roughness discontinuities. That means, that nearest to the wall a region exists which shows no or very small influence of the secondary flow. There is no numerical evidence that this region is only limited to the viscous sublayer.

3.2.3 Temperature statistics

The effect of the lateral roughness discontinuities on the temperature field can hardly be estimated. In the rough region one would expect an augmentation of the heat transfer rate, so that the internally heated air should be cooler in this region. But from the temperature field shown in Fig. 7 and the corresponding profiles in Fig. 12 one can see, that the temperature field is rather unaffected by the roughness. The secondary flow carries

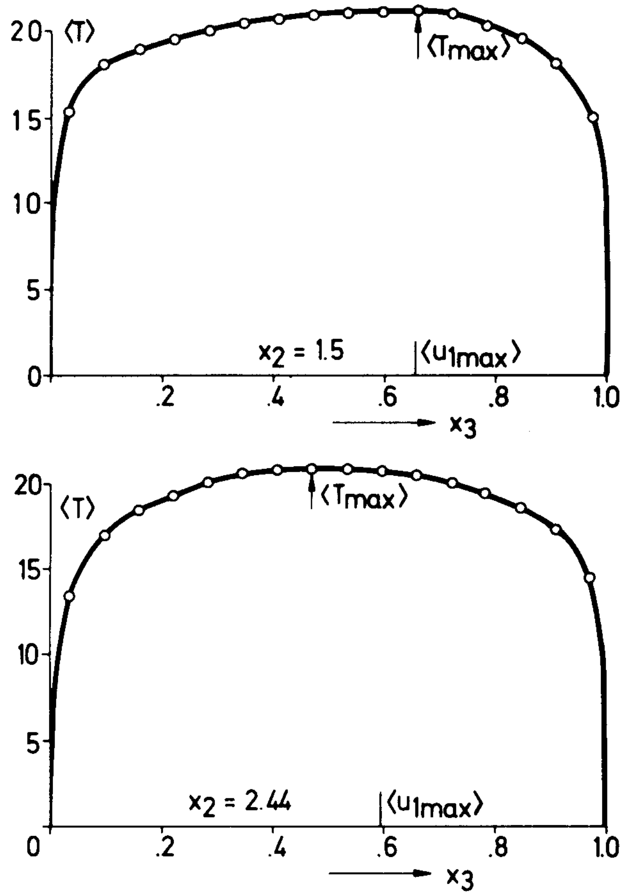

Fig. 12:
Time mean temperature profile in the smooth and rough region.

fluid with high temperature from the middle of the channel to the rough wall, and cooler fluid from the rough wall to the smooth wall and to the plane of symmetry. Thus the temperature differences within the fluid are largely compensated. The same holds also for the rms-values of the temperature fluctuations (Fig. 13) and for the radial turbulent heat flux (Fig. 14). Compared to the velocity fluctuations (Fig. 9), the temperature fluctuations in the rough and smooth regions are not very different, being only a little larger near the rough wall. Except for the displacement of the positions of the minimum fluctuations and for the zero turbulent heat flux these profiles are rather unaffected by the roughness discontinuities and the secondary flow. Nevertheless the turbulent heat

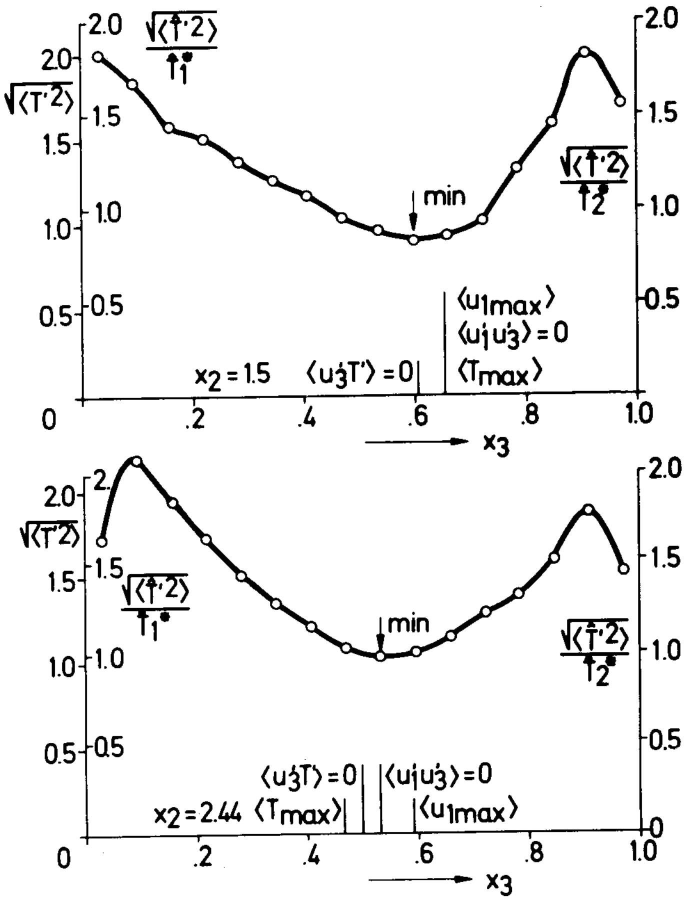

Fig. 13:
Root-mean-square temperature fluctuations in the smooth (x_2 = 1.5) and rough (x_2 = 2.44) region of the K8-Hinze channel.

flux profiles show the typical curvature mainly correlated with the local cross stream velocity (Fig. 8). The temperature fluctuations are therefore transportable physical quantities as well, but the influence of the secondary currents upon them is not so distinct as on the velocity fluctuations.

The wall heat flux profile calculated from the numerical results by proper averaging the logarithmic temperature profile (1, 23) shows a similar dependency (Fig. 15) on the wall roughness discontinuities as the wall shear stress. This is mainly due to the interconection represented by equation (23 l.h.s.). The wall heat flux $\dot{q}_{wl}$ at the partly roughened wall is weakly ascending in the direction to the plane of symmetry, that means in the direction of the secondary flow near this wall (see Fig. 7). From this behaviour one may conclude that nearest to the wall a region exists which shows a very small influence of the secondary flow only.

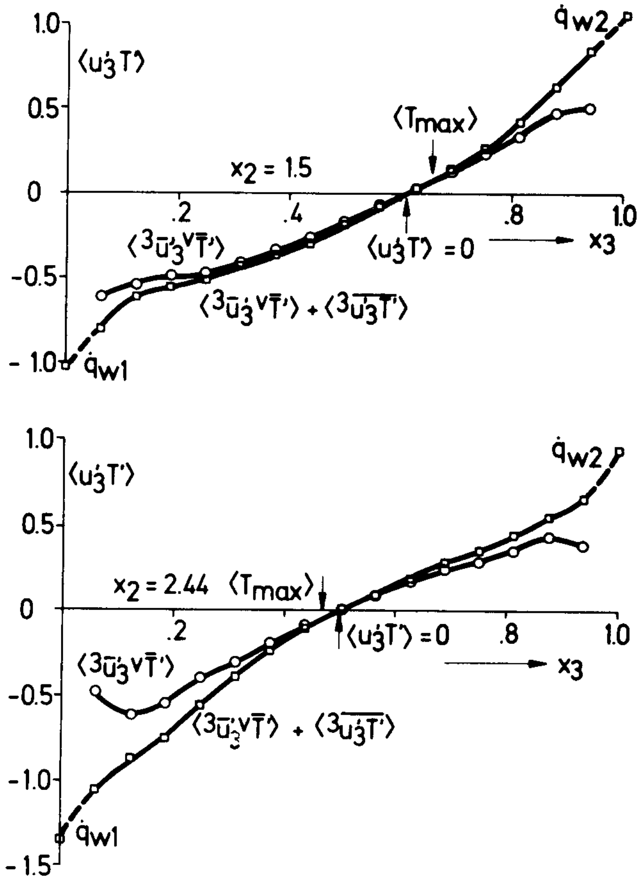

Fig. 14:
Radial turbulent heat flux $\langle u_3' T' \rangle$ as sum of the directly resolved part $\langle {}^3\overline{u_3}', {}^v\overline{T}' \rangle$ and the time mean part of the SGS model.

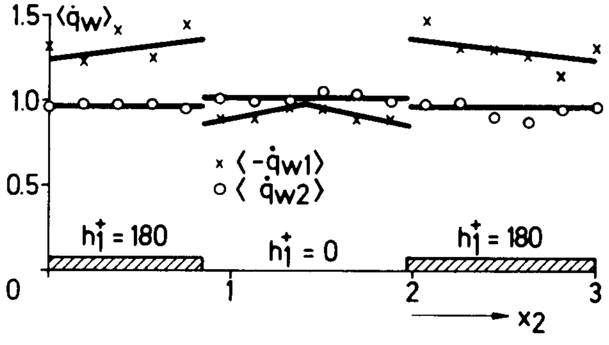

Fig. 15:
Wall heat flux profile at the partly roughened wall W1 and smooth wall W2.

3.2.4 Eddy diffusivities

From the results of the time dependent three-dimensional direct numerical simulation of turbulent flows one is not only able to calculate physical quantities like rms-values, shear stresses and heat fluxes, but also all quantities which are largely dominated by the resolved large scale structure. Quantities of large interest for most of the turbulence models are the turbulent eddy diffusivities ε_m and eddy conductivities ε_H, which can be calculated from the results given in the last two sections. Instead of the correct fourth- and second-order tensor notation /‾31, 32, 33_7 let introduce here the following generally known definitions:

$$\varepsilon_m = - \frac{<u_1' \; u_3'>}{\frac{\partial <u_1>}{\partial x_3}} \tag{24}$$

$$\varepsilon_H = - \frac{<u_3' \; T'>}{\frac{\partial <T>}{\partial x_3}} \tag{25}$$

The radial eddy diffusivity for momentum ε_m (24), calculated from the data shown in Fig. 8 and 10 is presented in Fig. 16. The eddy diffusivity is very small near the upper smooth wall, smaller than for smooth pipes

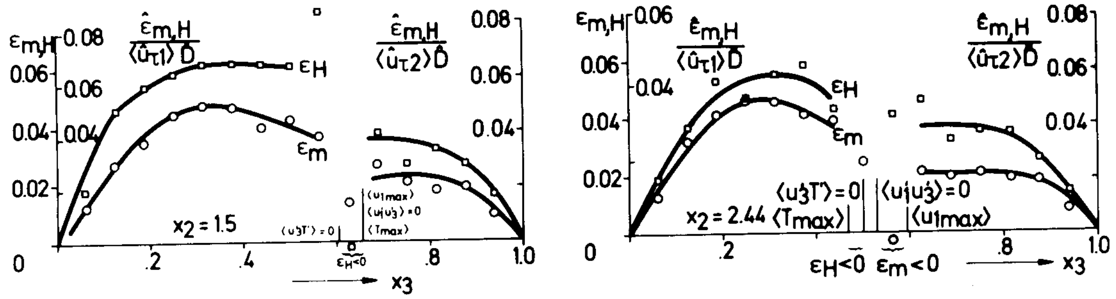

Fig. 16
Radial eddy diffusivity for momentum ε_m and heat ε_H in the rough (x_2 = 2.44) and smooth (x_2 = 1.5) region.

($\varepsilon_{m\ max} \simeq 0.04$), even when normalized with the local wall shear stress. Near the partly roughened wall (at $x_3 = 0$) ε_m is comparable to the pipe data in the rough region, but is somewhat greater in the smooth region. This is caused by the secondary flow, which carries fluid of high cross correlation from the rough wall to the plane of symmetry. By that means the highly turbulent boundary layer concentrated near the partly roughened wall in the plane of symmetry causes a very effective radial turbulent momentum exchange. For the lower wall the local wall shear stress of the rough region seems to be a good quantity to normalize the eddy diffusivity in the smooth region in order to get results which are comparable to pipe data (use the left inner nomenclature of the right profile for the left profile of Fig. 16. From this it is concluded, that the influence of the secondary flow on the velocity profile is different from that on the shear stress profile. Therefore the eddy diffusivity is not only a function of the geometry, but also a function of the secondary flow, except for the nearest region to the wall, as may be concluded from the small influence of the secondary flow on the wall shear stress distribution (Fig. 11). This implies that in the core of the flow field the eddy diffusivity for momentum is a transferable quantity as assumed in /‾34_7.

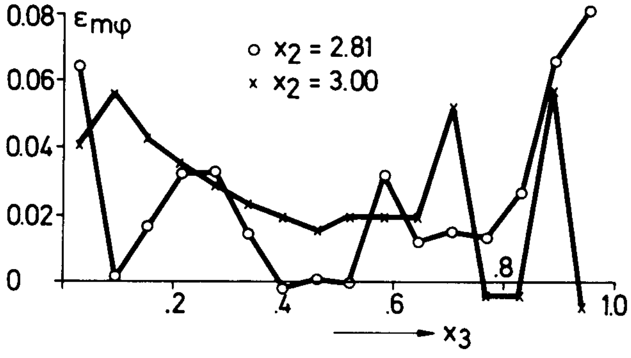

Fig. 17:
Lateral eddy diffusivity for momentum $\varepsilon_{m\phi}$ in the rough region.

The lateral eddy diffusivity for momentum $\varepsilon_{m\phi} = - \langle u_1' \, u_2' \rangle / (\partial \langle u_1 \rangle / \partial x_2)$, calculated from the numerical results given in Fig. 7, is shown in Fig. 17 for the positions $x_2 = 2.81$ and $x_2 = 3.0$ in the rough region. The scattering of the numerical data is very large, especially near the smooth wall, so that no conclusions can be drawn from these data. The reason for this consists in the fact that firstly $\varepsilon_{m\phi}$ is mostly dominated by small gradients $\partial\langle u_1\rangle/\partial x_2$, and secondly these small effects can only be estimated with sufficient accuracy using large time intervals for time averaging. The time interval realized (see Tab. 1) is too small to evaluate $\varepsilon_{m\phi}$ from the time dependent numerical results. Comparing the length, in units of the channel width, over which the fluid is transported meanwhile time averaging in experiments and in our numerical simulation, one can estimate that the computing time needed for comparable accuracy should be larger by a factor of about 10. Therefore only quantities which are less sensitive to short time averaging have been discussed here.

The radial eddy diffusivity for heat ε_H (25) calculated from the data shown in Fig. 12 and 14, is a little larger than that for momentum (Fig. 16). The influence of the secondary flow upon it seems to be nearly the same as on the eddy diffusivity for momentum. The resulting turbulent Prandtl-number $Pr_t = \varepsilon_m/\varepsilon_H$ averaged over the total channel is $\overline{Pr}_t = 0.74$. The positions of the zero fluxes and of the maxima of the velocity and temperature profiles are not always the same. Therefore one has not only to use negative eddy diffusivities in the regions between the locations of zero fluxes and corresponding maxima (see Fig. 16), but also to use negative turbulent Prandtl-numbers in regions, in which the eddy diffusivities are of different sign.

Except for this sign change caused by the smaller influence of the secondary flow on the temperature statistics than on the velocity statistics the turbulent Prandtl-number is fairly unaffected. This means that the behaviour of ε_H and ε_m is nearly similar. One can therefore conclude that not only ε_m, but also ε_H is strongly dependent on the secondary flow. Regarding to the rather unaffected wall shear stress distribution (Fig. 11) and wall heat flux distribution (Fig. 15), one may conclude, that close to the wall both radial eddy diffusivities show no or small influence of the secondary flow.

4. Conclusions

An extended version of the method of direct numerical simulation of turbulent flows has been used to study the effect of wall roughness on flow phenomena. The subgrid scale models used include the wall roughness effects in a consistent manner. No special additional assumptions have been introduced to account for wall roughness and secondary current effects. In addition, the same values of the correction factors have been used as determined earlier for smooth channels.

For verification of the computer code TURBIT-2 for rough channels the turbulent flow through a channel with one smooth and one rough wall has been calculated. Most of the quantities evaluated from the time dependent three-dimensional simulation agree with the experimental results within 5 %. This accuracy is remarkable because of the coarse grid used.

To study the influence of secondary flows the turbulent flow of air through a channel with lateral roughness discontinuities has been simulated. The method predicts successfully secondary flows. In accordance with experimental results the mean velocity field, the rms-values of the velocity fluctuations and the shear stress profiles in the plane of symmetry show strong distortions caused by the secondary flow. The numerical results for other planes within the channel show that these distortions are strongly correlated with the secondary flow. This is not only true for the velocity statistics, but also for the temperature, temperature fluctuations and turbulent heat flux fields. The radial eddy diffusivities calculated from the time dependent simulated turbulence are strongly affected by the secondary flow. Regarding to the lateral eddy diffusivities no conclusions may be drawn due to statistical errors caused by short time averaging. The turbulent Prandtl-number seems to be unaffected by the secondary flow, except for the occurrence of small regions where it takes negative values.

Acknowledgements:

The author wishes to thank Mr. W. Baumann for making available his experimental results, Dr. U. Schumann and Dr. K. Rehme for many usefull discussions. The comments of Dr. M. Bottoni and Dr. R. Meyder are also kindly acknowledged. Miss U. Stutz prepared the illustrations and Mrs. H. Jansky typed the manuscript. To all those who gave aid to this work, a truly heartfelt thank you.

5. Nomenclature

Operator notation for any quantity Y:

Y	any dimensionless quantity
$\hat{Y}$	any dimensional quantity
${}^{v}\overline{Y}$	volume mean value (eq. 1)
${}^{j}\overline{Y}$	surface mean value for the surface ${}^{j}F$ with the normal in the x_j-direction (eq. 2)
$\langle Y \rangle$	time mean value
Y'	deviation from a mean value
${}^{v}\overline{Y'}$	volume mean value of the subgrid scale structure
δ_j	finite difference operator in the x_j-direction (eq. 2)

Latin symbols

a	thermal diffusivity, ${}^{j}a_t$ isotropic, ${}^{j}a_t^{*}$ inhomogeneous part (eq. 8, 11, 13)
C_j	subgrid scale coefficients for momentum (eq. 10, 18)
C_{Tj}	subgrid scale coefficients for heat (temperature) (eq. 11)
c_f	friction factor (eq. 6)
c_p	specific heat at constant pressure
D	channel width ($2\,D = D_{hydr.}$)
E	kinetic energy
${}^{j}F$	surface area of a grid surface with the normal in the x_j-direction
h	characteristic width of grid cell (eq. 19), height of sand grain roughness
IM	number of grid cells in the x_1-direction (Fig. 1)
JM	number of grid cells in the x_2-direction

KM	number of grid cells in the x_3-direction
l	mixing length
Min(a,b)	Minimum between a and b (Min(a,b) = a for a < b and vice versa)
p	turbulent fluctuating pressure
P_x	time mean pressure gradient in the x_1-direction
Pr	molecular Prandtl number, $Pr = \hat{\nu}/\hat{a}$
$\dot{q}$	heat flux
$\dot{Q}$	volumetrical heat source
Re	Reynolds number $Re = {}^{V}\langle\hat{u}_1\rangle\,\hat{D}/\hat{\nu}$, ${}^{V}\langle\hat{u}_1\rangle$ bulk velocity
Re_τ	Reynolds number $Re_\tau = \langle\hat{u}_\tau\rangle\,\hat{D}/\hat{\nu}$
T	temperature
T^+	dimensionless temperature $T^+ = \langle\hat{T} - \hat{T}_W\rangle/\hat{T}^*$
T^*	friction temperature $\hat{T}^* = \hat{\dot{q}}_W/(\hat{\rho}\;\hat{c}_p\;\hat{u}_\tau)$
u_j	velocity component in the x_j-direction
u^+	dimensionless velocity $u^+ = \langle\hat{u}_1\rangle/\hat{u}_\tau$
u_τ	friction velocity $\hat{u}_\tau = \sqrt{\hat{\tau}_W/\hat{\rho}}$
x_j	coordinate (Fig. 1)
Δx_j	width of grid cell in the x_j-direction
X_j	periodicity length in the x_j-direction (Fig. 1)
y	distance from the wall
y^+	dimensionless distance from the wall $y^+ = \hat{y}\cdot Re_\tau/\hat{D}$

Greek symbols

δ_{ij}	Kronecker Delta
Δ	contour-line increment
ε	dissipation, eddy diffusivity (eq. 18, 24, 25)
μ	turbulent viscosity, ${}^{ij}\mu$ isotropic, ${}^{ij}\mu^*$ inhomogeneous (eq. 7, 10, 12)

ν	kinematic viscosity (dimensionless: $\nu \equiv 1/Re_\tau$)
ρ	density
τ	shear stress

Indices

1, 2	number of walls
D	calculated using the channel width $\hat{D}$
H	heat transfer
i, j	indices of the direction in the coordinate system
m	momentum
res	resolved part
t	turbulent
tot	resolved + subgrid scale part
W	wall
ϕ	lateral (x_2-) direction

6. Literature

1 Deardorff, J.W.: A numerical study of three-dimensional turbulent channel flow at large Reynolds-numbers. Journal of Fluid Mechanics, 41 (1970) p. 453-480

2 Schumann, U.: Sub grid scale model for finite difference simulations of turbulent flows in plane channels and annuli. Journal of Computational Physics, 18 (1975) p. 376-404

3 Grötzbach, G.: Direkte numerische Simulation turbulenter Geschwindigkeits-, Druck- und Temperaturfelder in Kanalströmungen. KFK 2426 (1977)

4 Grötzbach, G., Schumann, U.: Direct numerical simulation of turbulent velocity-, pressure- and temperature-fields in channel flows. Symposium on turbulent shear flows, Pennsylvania State University, 18.-20.4.1977, Proc. Editor: Durst, F., Schmidt, F.W., Whitelaw, J.H., Launder, B.E., Springer 1978, in press

5 Grötzbach, G.: Numerische Experimente zur Untersuchung des Wärmetransports in turbulenter Flüssigmetallströmung. Reaktortagung Mannheim, 29.3.-1.4.1977, p. 7-10

6 Meyder, R.: Turbulent velocity and temperature distribution in the central subchannel of rod bundles. Nuclear Engineering and Design, 35 (1975) p. 181-189

7 Ramm, H., Johannsen, K.: A phenomenological turbulence model and its application to heat transport in infinite rod arrays with axial turbulent flow. Journal of Heat Transfer, 97 (1975), p. 231-237

8 Nijsing, R., Eifler, W.: Temperature fields in liquid-metal-cooled rod assemblies. Progress in Heat and Mass Transfer, Vol. 7, Pergamon Press (1973) p. 115-149

9 Nagel, H.: Theoretische Untersuchung der Strömung und des Wärmetransports bei erzwungener turbulenter Konvektion im Rechteckkanal unter Berücksichtigung von Sekundäreffekten. Thesis, Technische Universität Berlin, TUBIK 52 (1976)

10 Naot, D., Shavit, A., Wolfshtein, M.: Numerical calculation of Reynolds stresses in a square duct with secondary flow. Wärme- und Stoffübertragung, 7 (1974) p. 151-161

11 Tracy, H.J.: Turbulent flow in a three-dimensional channel. Journal of Hydraulics Division, 91 (1965), No. HY 6, p. 9-35

12 Brundrett, E., Burroughs, P.R.: The temperature inner-law and heat transfer for turbulent air flow in a vertical square duct. International Journal of Heat and Mass Transfer, 10 (1967) p. 1133-1142

13 Wang, H., Nickerson, E.C.: Response of a turbulent boundary layer to lateral roughness discontinuities. Col. St. University, Fort Collins, Col., CER71-72HW-ECN51, THEMIS-Report No. 18 (1972)

14 Hinze, J.O.: Experimental investigation on secondary currents in the turbulent flow through a straight conduit. Applied Science Research, 28 (1973) p. 453-465

15 Grötzbach, G.: Untersuchung der Austauschkoeffizienten für Impuls und Enthalpie in turbulenter Kanalströmung. PSB-Vierteljahresbericht, KFK 1274/3, p. 129-1 - 129-9 (1974)

16 Eckelmann, H.: The structure of the viscous sublayer and the adjacent wall region in a turbulent channel flow. Journal of Fluid Mechanics, 65 (1974) p. 439-459

17 Baumann, W.: Personal communication, 28.4. + 12.11.1976

18 Baumann, W., Roth, A.: Experimentelle Untersuchungen an künstlichen Rauhigkeiten im Übergangsgebiet glatt-rauh. PSB-Vierteljahresbericht, KFK 1276/1, p. 127-6 - 127-10 (1976)

19 Baumann, W., Roth, A.: Strömungstechnische Untersuchungen an künstlichen Rauhigkeiten im Übergangsgebiet glatt-rauh. PSB-Vierteljahresbericht, KFK 1276/3, p. 127-1 - 127-5 (1976)

20 Maubach, K.: Reibungsgesetze turbulenter Strömungen in geschlossenen, glatten und rauhen Kanälen von beliebigem Querschnitt. KFK-Ext-4/69-22 (1969)

21 Grötzbach, G.: Erste Ergebnisse der direkten numerischen Simulation von Temperaturfeldern bei turbulenter Natriumströmung. PSB-Vierteljahresbericht, KFK 1276/2, p. 129-6 - 129-11 (1976)

22 Hanjalić, K., Launder, B.E.: Fully developed asymmetric flow in a plane channel. Journal of Fluid Mechanics, 71 (1972) p. 301-335

23 Rehme, K.: Turbulente Strömung in konzentrischen Ringspalten. KFK 2099 (1975)

24 Lawn, C.J.: Application of the turbulence energy equation to fully developed flow in simple ducts. CEGB-Report RD/B/R1575(a,b,c) (1970)

25 Grötzbach, G.: Direct numerical simulation of secondary currents in turbulent channel flows. Proceedings of the Symposium on Turbulence, Berlin, Aug. 1-5, 1977, Lecture Notes in Physics, Springer, in press

26 Kirsch, D.: Untersuchungen zur Strömungs- und Temperaturverteilung im Bereich lokaler Kühlkanalblockaden in Stabbündel-Brennelementen. KFK 1794 (1973)

27 Kirsch, D.: Investigations on the flow and temperature distribution downstream of local coolant blockages in rod bundle subassemblies. Nuclear Engineering and Design, 31 (1974) p. 266-279

28 Trupp, A.C., Azad, R.S.: The structure of turbulent flow in triangular array rod bundles. Nuclear Engineering and Design, 32 (1975) p. 47-84

29 Rehme, K.: Experimentelle Untersuchungen der turbulenten Strömung in einem Wandkanal eines Stabbündels. KFK 2441 (1977)

30 Vasanta Ram, V., Kiske, S.: An investigation into the relaxation process following a stepwise change in wall roughness in turbulent channel flow. Proceedings of Symposium on Turbulence, Berlin, Aug. 1-5, 1977, Lecture Notes in Physics, Springer, in press

31 Hinze, J.O.: Turbulence, Mc.Graw Hill, New York (1959)

32 Corrsin, S.: Limitations of gradient transport models in random walks and in turbulence. Advances in Geophysics 18A, Academic Press 1974, p. 25-60

33 Meyder, R.: Bestimmung des turbulenten Geschwindigkeits- und Temperaturfeldes in Stabbündeln mit Hilfe von krummlinig orthogonalen Koordinaten. KFK 2029 (1974)

34 Nee, V.W., Kovasznay, L.S.G.: Simple phenomenological theory of turbulent shear flows. Physics of Fluids, 12 (1969), p. 473-484

7. Appendix

TURBIT-2-Plotoutput for the channel with one constant roughened wall (K7-Baumann)

To show the capabilities of direct numerical simulation method for turbulent flows the complete profile - plotoutput of the TURBIT-2-analyzing program is included here for the constant roughened K7-Baumann channel. The data are averaged over the time dependent three-dimensional results from $t_o = 7.795$ to $t = 9.543$ using the results at 13 different time steps only. (The number of data sets used is restricted by the practicability of storing the time dependent 3-d fields on magnetic tapes, especially when rather large meshes are used.) Some of the profiles appear twice because of using different time averaging technics (Fig. 8, 40; 10, 41; 35, 38; 37, 39), or depending on whether the subgrid scale parts are included (Fig. 37, 39) or not (Fig. 32). In addition to the nomenclature given in chapter 5 the following symbols have to be added:

A_{ij}	constants in the Rotta-pressure strain model (i,j = 1,2,3), for Ref. see [3] $\langle p' (\frac{\partial u'_i}{\partial x_j} + \frac{\partial u'_j}{\partial x_i})\rangle = - A_{ij} \frac{\varepsilon}{E_{tot}} (\langle u'_i u'_j\rangle - \frac{2}{3} \delta_{ij} E_{tot})$
C_{iT}	constant in the Launder-pressure scrambling model (i = 1,2), for Ref. see [3] $\langle p' \frac{\partial T'}{\partial x_j}\rangle = - C_{1T} \frac{\varepsilon}{E_{tot}} \langle u'_j T'\rangle + C_{2T} \langle u'_i T'\rangle \frac{\partial \langle u_j\rangle}{\partial x_i}$
E_{ii}	energy spectra, calculated from the space-dependent data
K_1	one-dimensional wave number
$L_{ij,k}$	correlation length of R_{ij} $(\underline{x}_k)$ in the $\underline{x}_k$-direction $= \frac{2}{X_k} \int_0^{X_k/2} R_{ij} (\underline{x}_k)\, d\underline{x}_k$
R_{ij} $(\underline{x}_k)$	two-point correlation $= \frac{\langle u'_i(\underline{x}) u'_j(\underline{x}+\underline{x}_k)\rangle}{\langle u'_i(\underline{x}) u'_j(\underline{x})\rangle}$
(VZ,VP,VR)	velocity vector $= (u_1, u_2, u_3) = (u, v, w) = \underline{u}$
$\underline{x}_j$	translation vector $= (x_1, 0, 0)$ $j = 1$ $= (0, x_2, 0)$ $j = 2$ $= (0, 0, x_3)$ $j = 3$

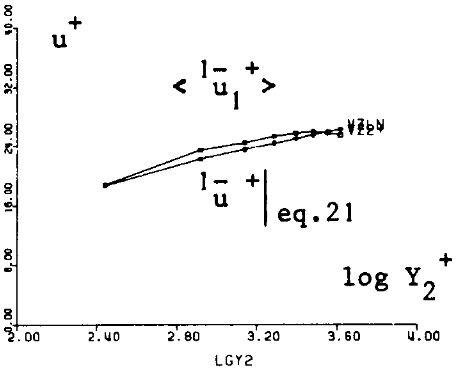

ABB.3 T= 9.543 K7 BAUMANN TO=7.79

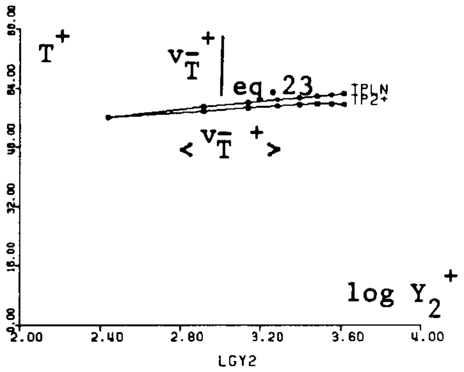

ABB.6 T= 9.543 K7 BAUMANN TO=7.79

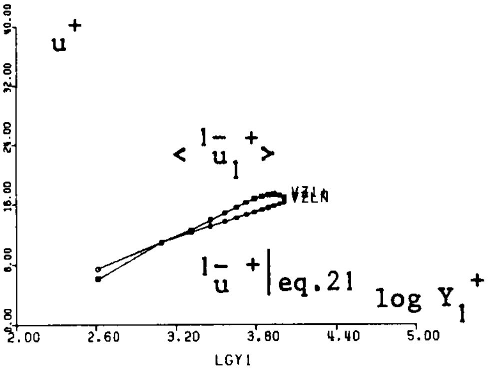

ABB.2 T= 9.543 K7 BAUMANN TO=7.79

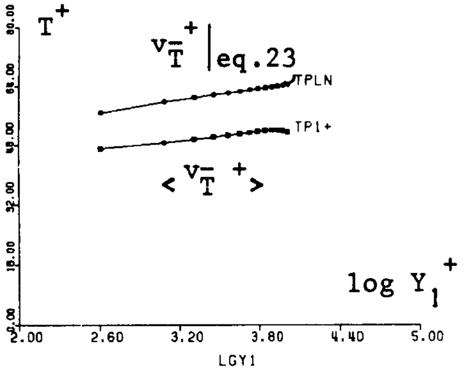

ABB.5 T= 9.543 K7 BAUMANN TO=7.79

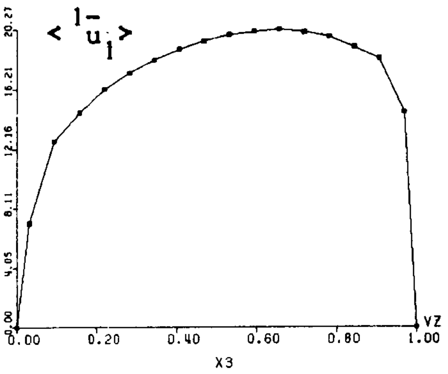

ABB.1 T= 9.543 K7 BAUMANN TO=7.79

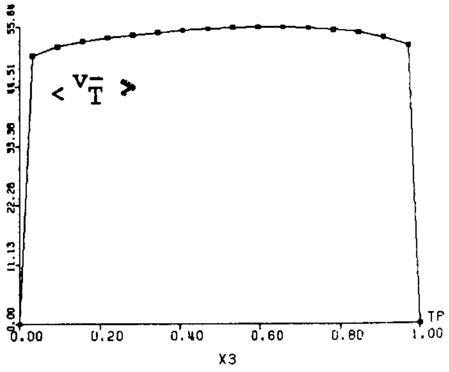

ABB.4 T= 9.543 K7 BAUMANN TO=7.79

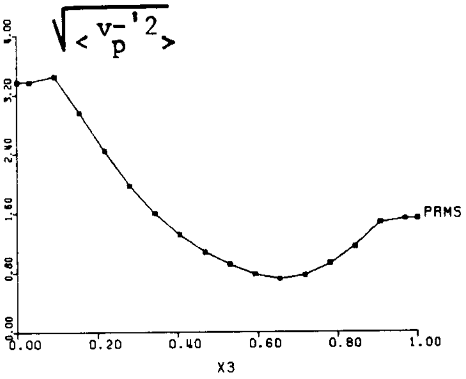

ABB.9 T= 9.543 K7 BAUMANN T0=7.79

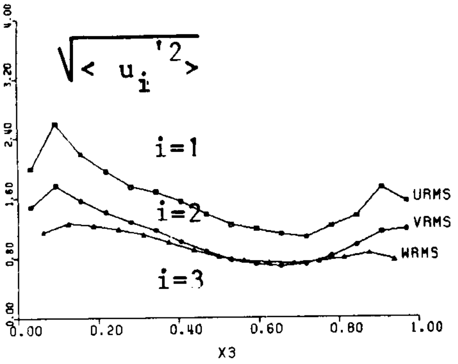

ABB.8 T= 9.543 K7 BAUMANN T0=7.79

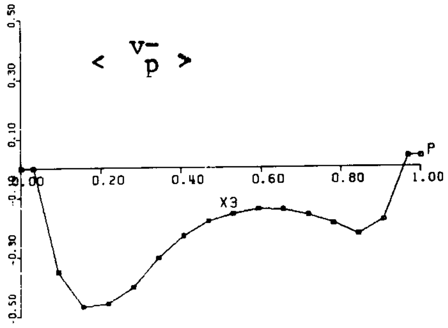

ABB.7 T= 9.543 K7 BAUMANN T0=7.79

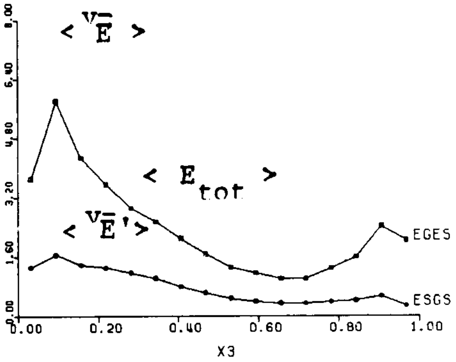

ABB.12 T= 9.543 K7 BAUMANN T0=7.79

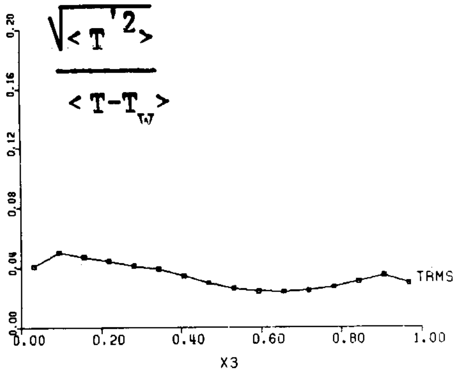

ABB.11 T= 9.543 K7 BAUMANN T0=7.79

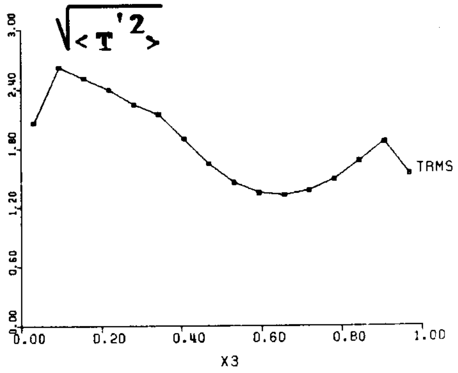

ABB.10 T= 9.543 K7 BAUMANN T0=7.79

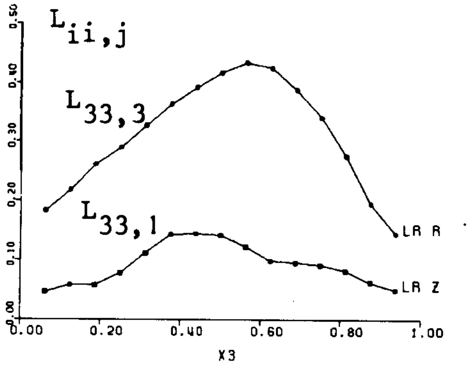

ABB.15 T= 9.543 K7 BAUMANN TO=7.79

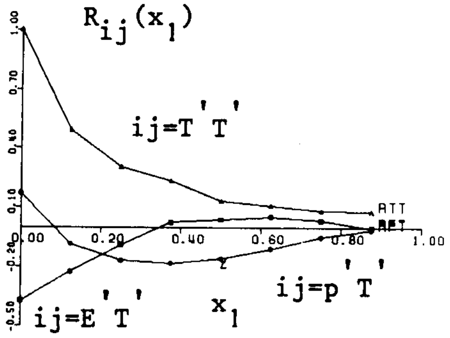

ABB.18 T= 9.543 K7 BAUMANN TO=7.79

$Y_1 = 0.4688$

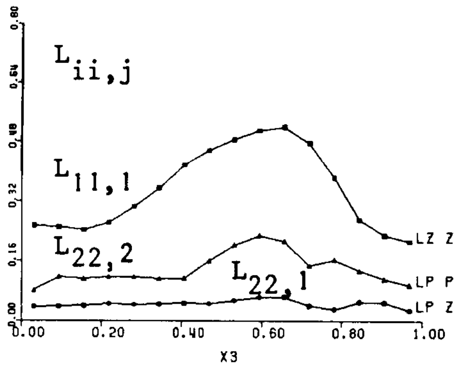

ABB.14 T= 9.543 K7 BAUMANN TO=7.79

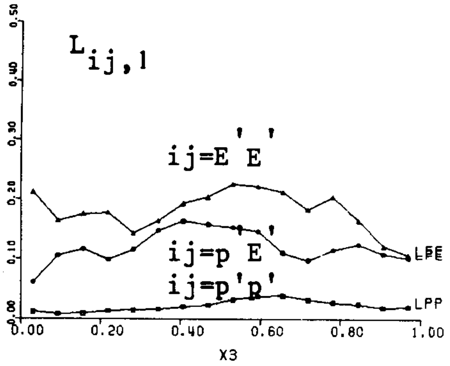

ABB.17 T= 9.543 K7 BAUMANN TO=7.79

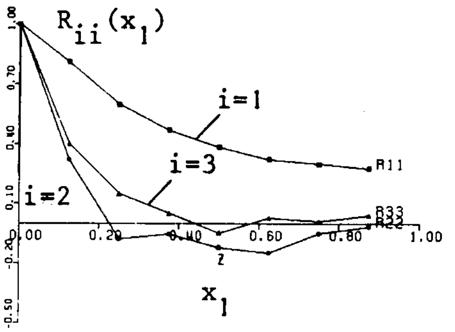

ABB.13 T= 9.543 K7 BAUMANN TO=7.79

$Y_1 = 0.4688$

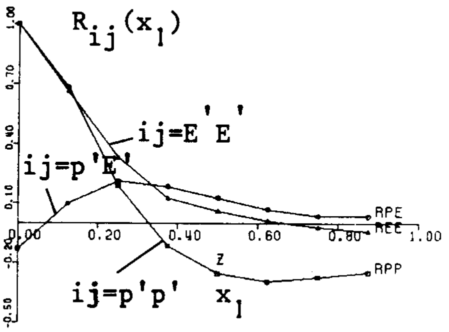

ABB.16 T= 9.543 K7 BAUMANN TO=7.79

$Y_1 = 0.4688$

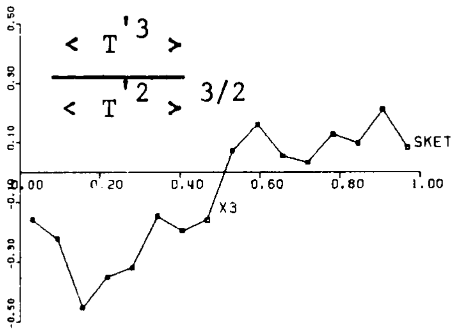

ABB.21 T= 9.543 K7 BAUMANN TO=7.79

Skewness

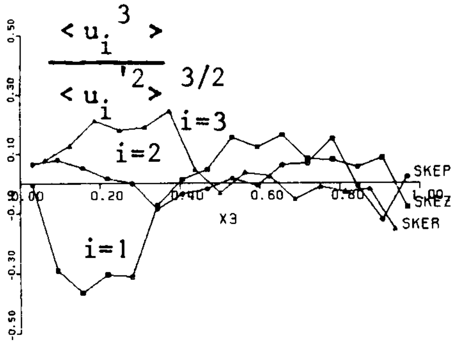

ABB.20 T= 9.543 K7 BAUMANN TO=7.79

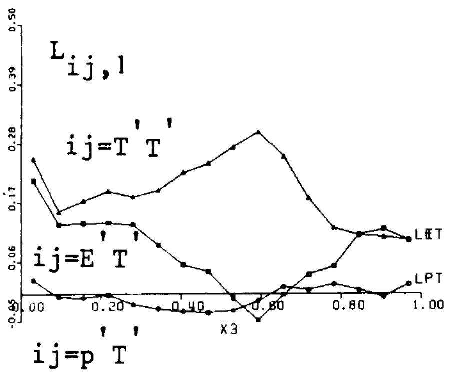

ABB.19 T= 9.543 K7 BAUMANN TO=7.79

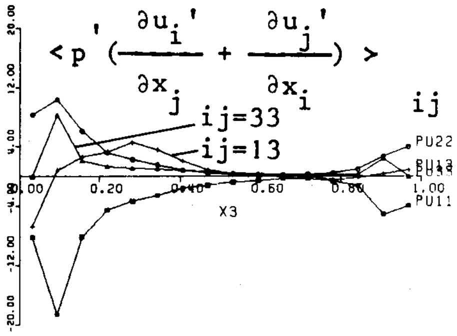

ABB.24 T= 9.543 K7 BAUMANN TO=7.79

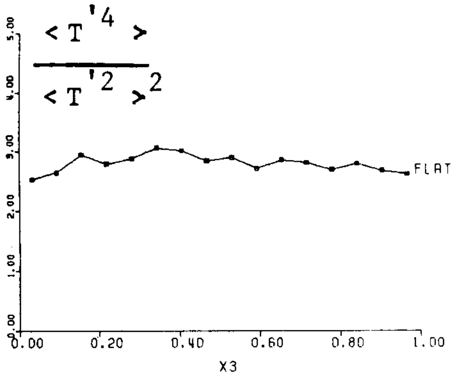

ABB.23 T= 9.543 K7 BAUMANN TO=7.79

Flatness

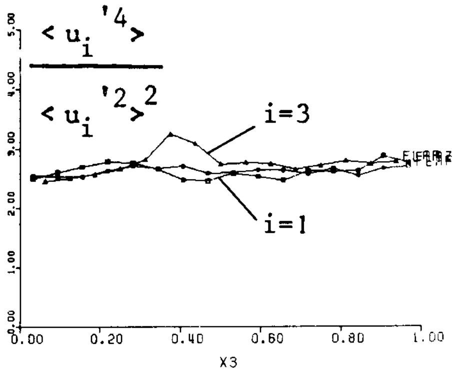

ABB.22 T= 9.543 K7 BAUMANN TO=7.79

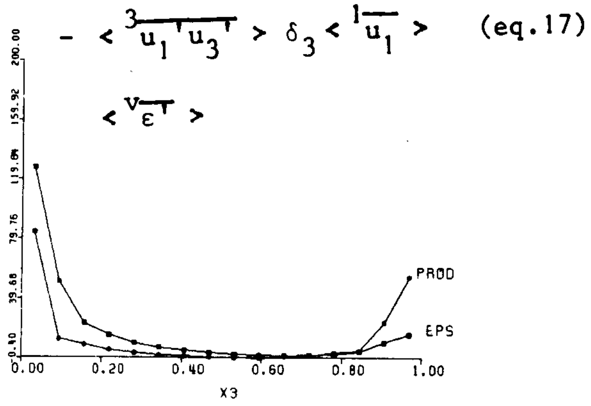

ABB.27 T= 9.543 K7 BAUMANN TO=7.79

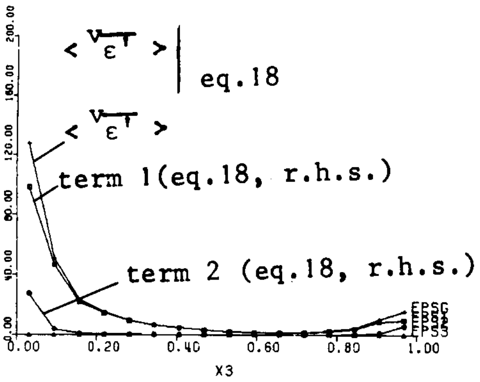

ABB.26 T= 9.543 K7 BAUMANN TO=7.79

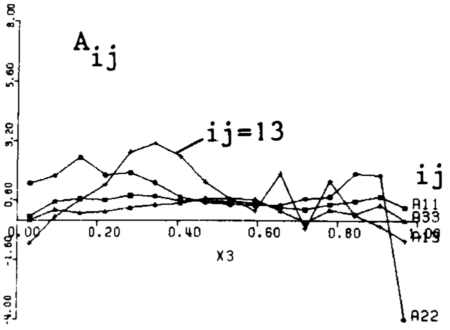

ABB.25 T= 9.543 K7 BAUMANN TO=7.79

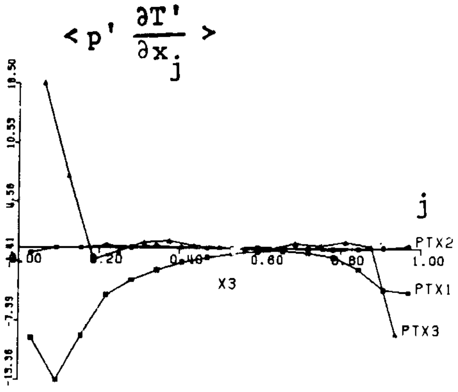

ABB.30 T= 9.543 K7 BAUMANN TO=7.79

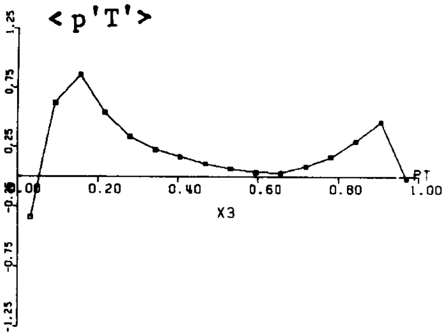

ABB.29 T= 9.543 K7 BAUMANN TO=7.79

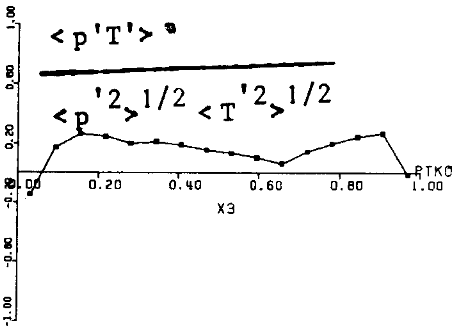

ABB.28 T= 9.543 K7 BAUMANN TO=7.79

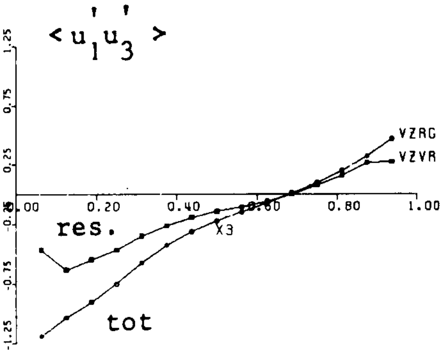

ABB.33 T= 9.543 K7 BAUMANN TO=7.79

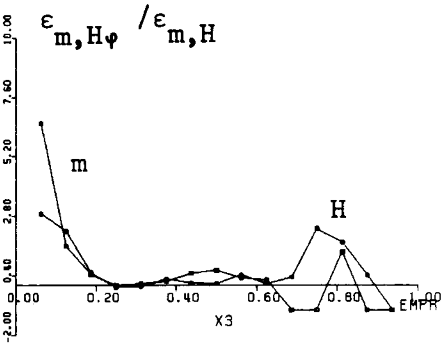

ABB.36 T= 9.543 K7 BAUMANN TO=7.79

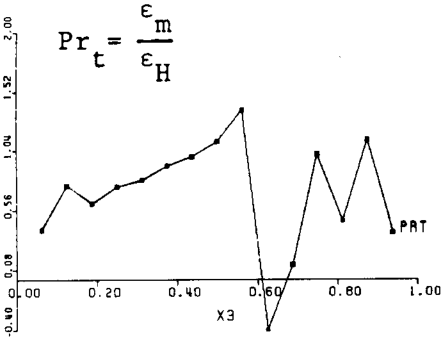

ABB.32 T= 9.543 K7 BAUMANN TO=7.79

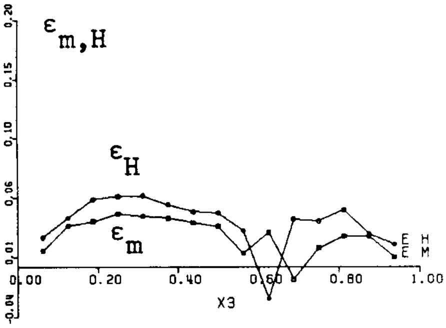

ABB.35 T= 9.543 K7 BAUMANN TO=7.79

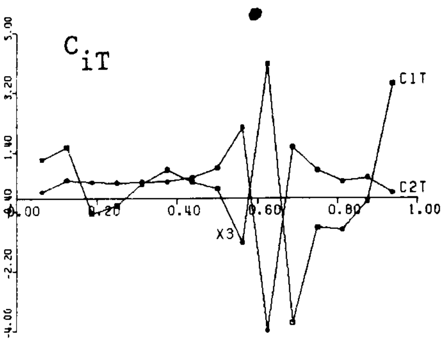

ABB.31 T= 9.543 K7 BAUMANN TO=7.79

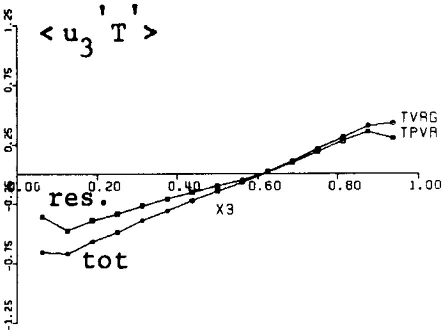

ABB.34 T= 9.543 K7 BAUMANN TO=7.79

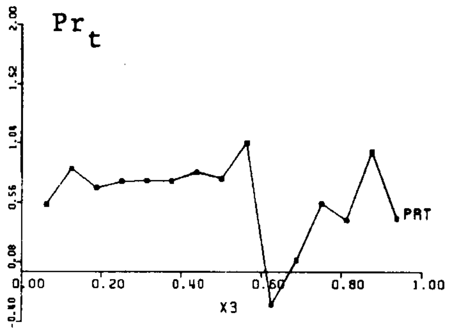

ABB.39 T= 9.543 K7 BAUMANN T0=7.79

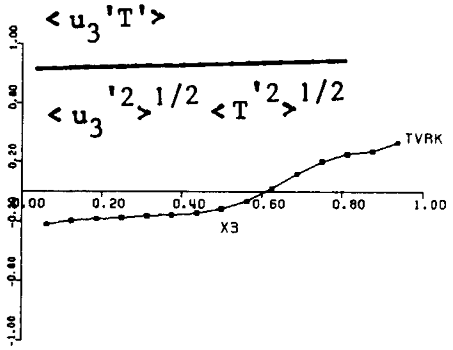

ABB.42 T= 9.543 K7 BAUMANN T0=7.79

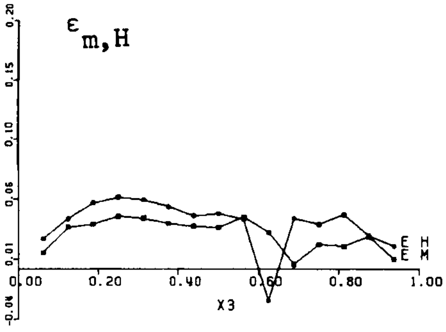

ABB.38 T= 9.543 K7 BAUMANN T0=7.79

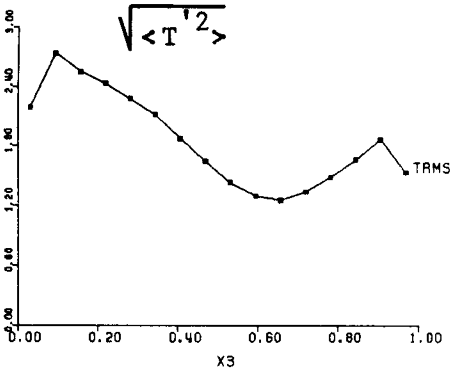

ABB.41 T= 9.543 K7 BAUMANN T0=7.79

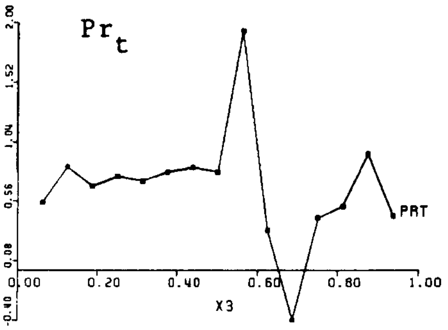

ABB.37 T= 9.543 K7 BAUMANN T0=7.79

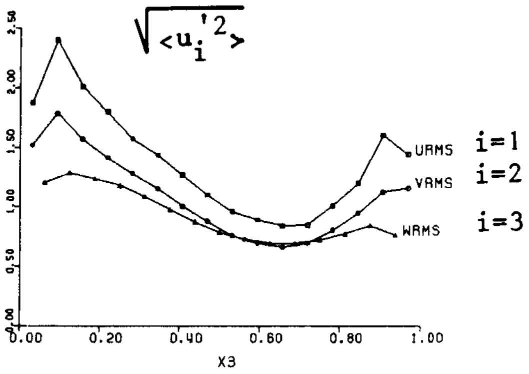

ABB.40 T= 9.543 K7 BAUMANN T0=7.79

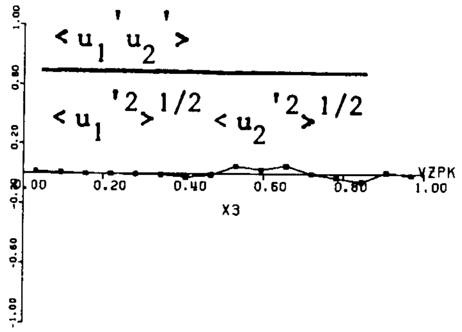

ABB.45 T= 9.543 K7 BAUMANN TO=7.79

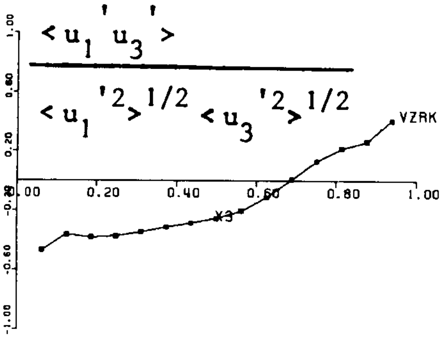

ABB.44 T= 9.543 K7 BAUMANN TO=7.79

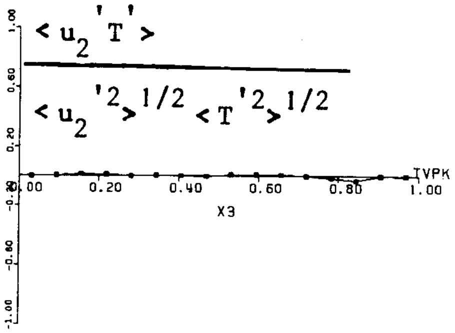

ABB.43 T= 9.543 K7 BAUMANN TO=7.79

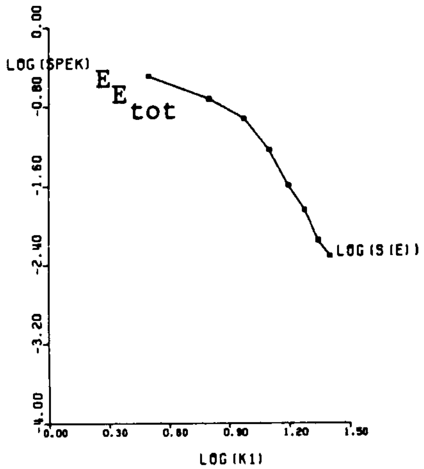

Abb.47 RAUMLICHES SPEKTRUM K= 2 T= 9.543 K7 BAUMANN

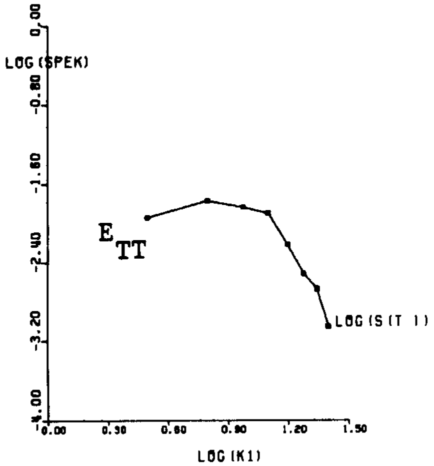

Abb.49 RAUMLICHES SPEKTRUM K= 2 T= 9.543 K7 BAUMANN

$\underline{Y_1 = 0.0935}$

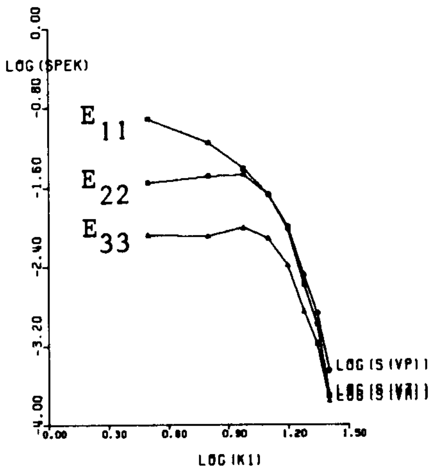

Abb.46 RAUMLICHES SPEKTRUM K= 2 T= 9.543 K7 BAUMANN

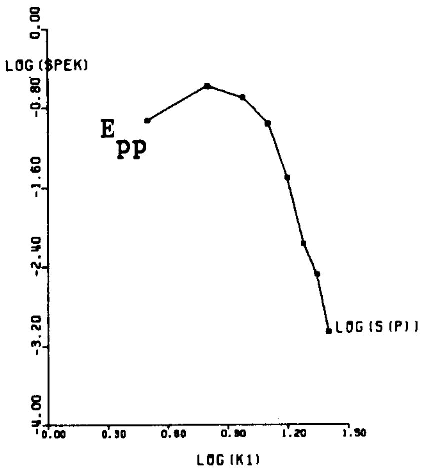

Abb.48 RAUMLICHES SPEKTRUM K= 2 T= 9.543 K7 BAUMANN

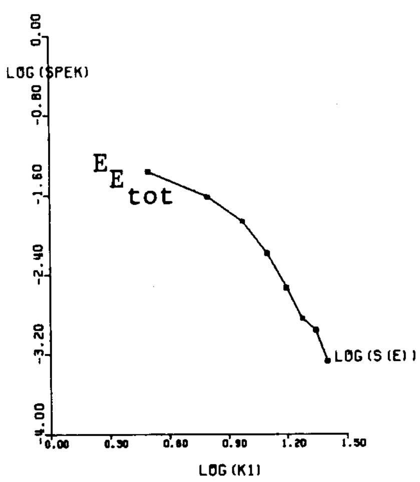

Abb.51 RAUMLICHES SPEKTRUM K= 8 T= 9.543 K7 BAUMANN

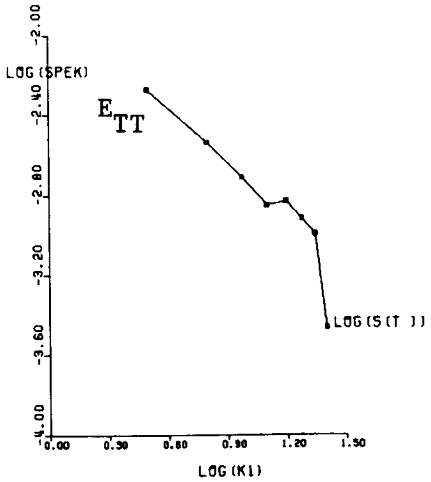

Abb.53 RAUMLICHES SPEKTRUM K= 8 T= 9.543 K7 BAUMANN

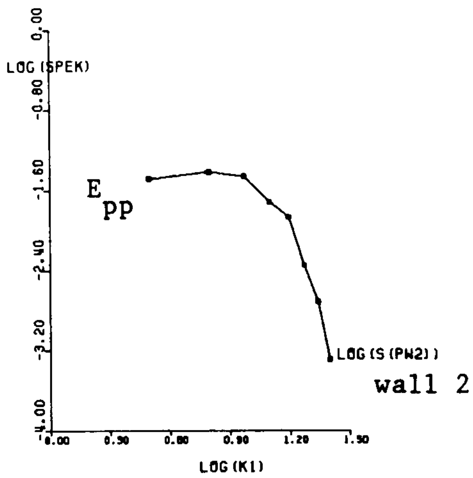

Abb.55 RAUMLICHES SPEKTRUM K= 17 T= 9.543

$\underline{Y_1 = 0.4688}$

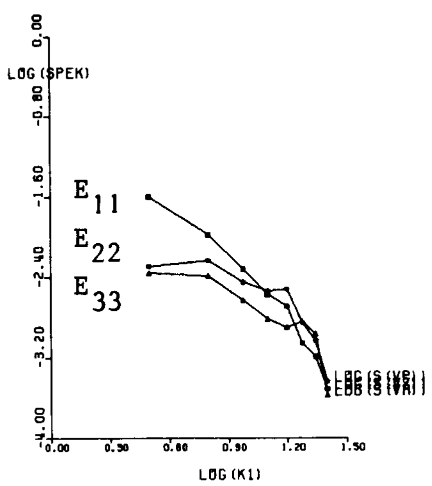

Abb.50 RAUMLICHES SPEKTRUM K= 8 T= 9.543 K7 BAUMANN

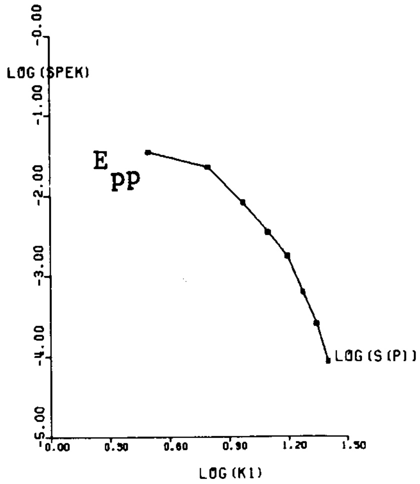

Abb.52 RAUMLICHES SPEKTRUM K= 8 T= 9.543 K7 BAUMANN

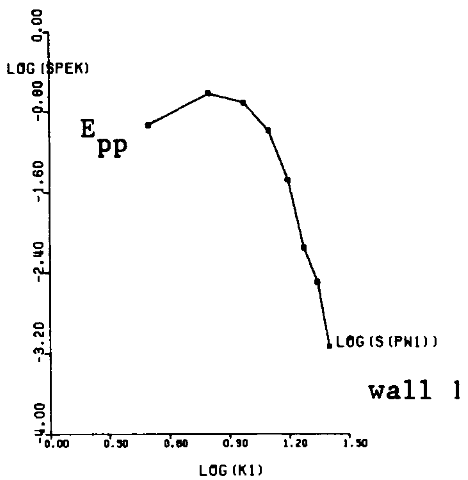

Abb.54 RAUMLICHES SPEKTRUM K= 0 T= 9.543